

## ACCESS: An optical transmission spectrum of the high-gravity, hot Jupiter HAT-P-23b

IAN C. WEAVER <sup>1</sup>, MERCEDES LÓPEZ-MORALES <sup>1</sup>, MUNAZZA K. ALAM <sup>1</sup>, NÉSTOR ESPINOZA <sup>2</sup>,  
BENJAMIN V. RACKHAM <sup>3,\*</sup>, JAYESH M. GOYAL <sup>4</sup>, RYAN J. MACDONALD <sup>4</sup>, NIKOLE K. LEWIS <sup>4</sup>,  
DÁNIEL APAI <sup>5,6,7</sup>, ALEX BIXEL <sup>8,6</sup>, ANDRÉS JORDÁN <sup>9,10</sup>, JAMES KIRK <sup>1</sup>, CHIMA MCGRUDER <sup>1</sup> AND  
DAVID J. OSIP<sup>11</sup>

<sup>1</sup>Center for Astrophysics | Harvard & Smithsonian, 60 Garden St, Cambridge, MA 02138, USA

<sup>2</sup>Space Telescope Science Institute, 3700 San Martin Drive, Baltimore, MD 21218, USA

<sup>3</sup>Department of Earth, Atmospheric and Planetary Sciences, and Kavli Institute for Astrophysics and Space Research, Massachusetts Institute of Technology, Cambridge, MA 02139, USA

<sup>4</sup>Department of Astronomy and Carl Sagan Institute, Cornell University, 122 Sciences Drive, 14853, Ithaca, NY, USA

<sup>5</sup>Department of Astronomy/Steward Observatory, The University of Arizona, 933 N. Cherry Avenue, Tucson, AZ 85721, USA

<sup>6</sup>Earths in Other Solar Systems Team, NASA Nexus for Exoplanet System Science

<sup>7</sup>Lunar and Planetary Laboratory, The University of Arizona, 1640 E. Univ. Blvd, Tucson, AZ 85721

<sup>8</sup>Department of Astronomy/Steward Observatory, The University of Arizona, 933 N. Cherry Avenue, Tucson, AZ 85721, USA

<sup>9</sup>Facultad de Ingeniería y Ciencias, Universidad Adolfo Ibáñez, Av. Diagonal las Torres 2640, Peñalolén, Santiago, Chile

<sup>10</sup>Millennium Institute for Astrophysics, Santiago, Chile

<sup>11</sup>Las Campanas Observatory, Carnegie Institution for Science, Colina el Pino, Casilla 601 La Serena, Chile

(Received 2021 February 12; Revised 2021 April 05; Accepted 2021 April 07)

### Abstract

We present a new ground-based visible transmission spectrum of the high-gravity, hot Jupiter HAT-P-23b, obtained as part of the ACCESS project. We derive the spectrum from five transits observed between 2016 and 2018, with combined wavelength coverage between 5,200 Å–9,269 Å in 200 Å bins, and with a median precision of 247 ppm per bin. HAT-P-23b’s relatively high surface gravity ( $g \approx 30 \text{ m/s}^2$ ), combined with updated stellar and planetary parameters from *Gaia* DR2, gives a 5-scale-height signal of 384 ppm for a hydrogen-dominated atmosphere. Bayesian models favor a clear atmosphere for the planet with the tentative presence of TiO, after simultaneously modeling stellar contamination, using spots parameter constraints from photometry. If confirmed, HAT-P-23b would be the first example of a high-gravity gas giant with a clear atmosphere observed in transmission at optical/NIR wavelengths; therefore, we recommend expanding observations to the UV and IR to confirm our results and further characterize this planet. This result demonstrates how combining transmission spectroscopy of exoplanet atmospheres with long-term photometric monitoring of the host stars can help disentangle the exoplanet and stellar activity signals.

**Keywords:** planets and satellites: atmospheres — planets and satellites: individual (HAT-P-23b) — stars: activity — stars: starspots — techniques: spectroscopic

### 1. INTRODUCTION

Observations of exoplanetary atmospheres offer the possibility of understanding the atmospheric physical properties and chemical composition of those worlds, as well as providing clues to their formation and evolution

histories (e.g., Öberg et al. 2013; Moses et al. 2013; Mordasini et al. 2016, Espinoza et al. 2017). The first comparative studies of exoplanetary atmospheres using transmission spectra (see, e.g., Sing et al. 2016) found evidence of a gradual transition between clear and cloudy atmospheres, but no clear correlation of that transition with other system parameters, such as planetary mass, gravity, effective temperature, or stellar irradiation levels, and the chemical composition of the star.

High-altitude clouds and hazes have been inferred in the atmosphere of a number of exoplanets from scattering slopes in the visible (e.g., Pont et al. 2008, 2013; Sing et al. 2009, 2011, 2013; Jordán et al. 2013; Gibson et al. 2013), and from the absence of the pressure-broadened alkali Na I and K I lines originating from deeper within the atmosphere (e.g., Charbonneau et al. 2002; Wakeford & Sing 2015). The first detections of gas giants with potentially clear atmospheres, as indicated by the presence of complete pressure-broadened alkali line profiles, have only recently been made, e.g., WASP-39b (Nikolov et al. 2016; Fischer et al. 2016; Wakeford et al. 2018; Kirk et al. 2019), WASP-96b (Nikolov et al. 2018), and WASP-62b (Alam et al. 2021).

A current driving focus of this field is identifying what system parameters may correlate with the observed atmospheric properties of exoplanets. For example, the relationship between chemical abundance in an exoplanet’s atmosphere and planet mass is actively being explored (e.g. Helling et al. 2016; Sing et al. 2016; Kreidberg et al. 2014; Fraine et al. 2014). Recently, Pinhas et al. (2019) reanalyzed the Sing et al. (2016) sample and concluded that the majority of hot Jupiters have atmospheres consistent with sub-solar H<sub>2</sub>O abundances. In addition, comparisons of H<sub>2</sub>O absorption vs. equilibrium temperature (Fu et al. 2017; Stevenson 2016), and cloudiness vs. irradiation and cloudiness vs. Na I/K I absorption (Heng 2016) have also been explored. The current population of exoplanets studied is still too limited to make any substantial claims regarding statistical correlations between the parameters explored in these studies, making continued work in exoplanet characterization extremely important for the future of comparative exoplanetology. Ground-based (e.g., ACCESS<sup>1</sup>, GPIES<sup>2</sup>, VLT FORS2<sup>3</sup>, LRG-BEASTS<sup>4</sup>) and space-based surveys (PanCET<sup>5</sup>) are working towards providing homogeneous spectra of statistically significant numbers of exoplanet atmospheres in the search for these parameter correlations.

For example, the population of high-gravity exoplanets offers a novel testing ground for planet interior and atmosphere studies. For transmission spectroscopy obser-

vations, we often rely on estimates of the scale height of a planet’s atmosphere to gauge the expected amplitude of the spectroscopic features. A planet’s atmospheric scale height ( $H$ ) is fundamentally tied to its surface gravity ( $g$ ), temperature ( $T$ ), and mean molecular weight ( $\mu$ ), by  $H = k_B T / \mu g$ . To date, there has been a strong preference to target exoplanets with large scale heights for transmission spectroscopy observations, which has resulted in the bulk of observational data that is focused on objects that are much lower gravity and much hotter than Jupiter ( $g \sim 25 \text{ m/s}^2$ ,  $T_{\text{eff}} \sim 150 \text{ K}$ ) in our own Solar System (see for example review by Sing 2018). Thus our view of the physics and chemistry at work in exoplanet atmospheres has been obscured by this biased sample. In particular, a planet’s gravity plays a key role in shaping its horizontal and vertical advection patterns (e.g., Showman et al. 2009) and the vertical extent of clouds in the atmosphere (e.g., Marley et al. 2013). Although technically challenging, the extension of the sample of exoplanets with transmission spectroscopy observations into the “high-gravity” regime will allow us to tease apart the physical processes shaping the atmospheres of these distant worlds. To date, the only exoplanets with surface gravities in excess of  $20 \text{ m/s}^2$  to be probed via transmission spectroscopy at optical-NIR wavelengths are HD 189733b ( $g \sim 23 \text{ m/s}^2$ ,  $T_{\text{eq}} \sim 1,200 \text{ K}$ ), WASP-43b ( $g \sim 47 \text{ m/s}^2$ ,  $T_{\text{eq}} \sim 1,440 \text{ K}$ ), and now HAT-P-23b ( $g \sim 31 \text{ m/s}^2$ ,  $T_{\text{eq}} \sim 2,000 \text{ K}$ ) with this work. In this paper, we present the ground-based visible transmission spectrum of the hot Jupiter HAT-P-23b, obtained as part of the ACCESS survey.

HAT-P-23b is a hot Jupiter discovered by Bakos et al. (2011) transiting the G0 star HAT-P-23 ( $M_s = 1.08 M_\odot \pm 0.14 M_\odot$ ,  $R_s = 1.152 R_\odot \pm 0.060 R_\odot$ ,  $T_{\text{eff}} = 5,920.0 \text{ K} \pm 140.0 \text{ K}$ ,  $V = 11.9$ ; Stassun et al. 2019). Assuming a circular orbit ( $e < 0.052$ ; Bonomo et al. 2017), and combining the most recent transit ( $R_p/R_s = 0.1113 \pm 0.001$ ,  $P = 1.2128867 \text{ days} \pm 0.0000002 \text{ days}$ ; Sada & Ramón-Fox 2016) and radial velocity observations ( $K_{\text{RV}} = 346 \text{ m/s} \pm 21 \text{ m/s}$ ,  $i = 85.1^\circ \pm 1.5^\circ$ ; Bonomo et al. 2017) with the updated stellar parameters from *Gaia* parallax measurements, Stassun et al. (2019) give self-consistent estimates<sup>6</sup> for the physical parameters of HAT-P-23b as  $M_p = 1.92 M_J \pm 0.20 M_J$ ,  $R_p = 1.247 R_J \pm 0.066 R_J$ ,  $T_{\text{eq}} = 2,027 \text{ K} \pm 92 \text{ K}$ , and  $\log g \text{ (cm/s}^2\text{)} = 3.485 \pm 0.064$ .

Previous multiband, photometric observations in the visible portion of the spectrum collected by the Bonn University Simultaneous Camera (BUSCA), mounted

<sup>1</sup>ACCESS, previously known as the Arizona-CfA-Católica-Carnegie Exoplanet Spectroscopy Survey (Rackham et al. 2017), has been renamed to the Atmospheric Characterization Collaboration for Exoplanet Spectroscopic Studies

<sup>2</sup>Gemini Planet Imager Extra Solar Survey (Nielsen et al. 2019)

<sup>3</sup>Very Large Telescope FOcal Reducer and Spectrograph (Nikolov et al. 2018)

<sup>4</sup>Low Resolution Ground-Based Exoplanet Atmosphere Survey using Transmission Spectroscopy (Kirk et al. 2018)

<sup>5</sup>Panchromatic Comparative Exoplanetology Treasury (Wakeford et al. 2017)

<sup>6</sup><https://icweaver.github.io/ExoCalc.jl/>

on the 2.2 m Calar Alto Telescope, indicate a flat transmission spectrum (Ciceri et al. 2015). Additionally, secondary eclipse data collected in  $H$  and  $K_s$  bands with the Wide-field Infrared Camera (WIRC) on the 200 inch Hale Telescope and in the  $3.6 \mu\text{m}$  and  $4.5 \mu\text{m}$  bands with the InfraRed Array Camera (IRAC) aboard Spitzer indicate a planetary atmosphere with low efficiency energy transport from its day-side to night-side, no thermal inversion, and a lack of strong absorption features (O’Rourke et al. 2014).

We use new transit observations on *Magellan/IMACS* to produce the visible spectrum spanning  $0.52 \mu\text{m}$ – $0.93 \mu\text{m}$ . We use this transmission spectrum to better constrain the abundance of Na I and K I, and search for the presence of clouds/hazes in the atmosphere in HAT-P-23b. In our analysis, we find that a clear planetary atmosphere containing TiO is marginally preferred over other models including stellar activity.

This paper is structured as follows. In Section 2 we present our *Magellan/IMACS* observations. In Section 3 we outline the data reduction process used in our observations. In Section 4 we discuss our detrending techniques and present the detrended white-light and binned light curves for each night. In Section 5 we investigate the impact of stellar activity. In Section 6 we present the final combined transmission spectrum, and in Section 7 we present the results of a forward modeling and retrieval analysis on this spectrum when the presence of a heterogeneous stellar photosphere is taken into account. We then summarize and conclude in Section 8. For convenience, we include links throughout the paper to Python code (</>) used to produce each figure, which is archived on Zenodo doi:10.5281/zenodo.4673489.

## 2. OBSERVATIONS

### 2.1. General setup

We observed five transits of HAT-P-23b between 2016 and 2018 with the 6.5-meter Magellan Baade Telescope and Inamori-Magellan Areal Camera and Spectrograph (IMACS, Dressler et al. 2006) as part of ACCESS, a multi-institutional effort to build a comparative library of visual transmission spectra of transiting exoplanets. For these observations, we used the IMACS f/2 camera. This camera has a  $27.4'$  diameter field of view (FoV), in which we can observe simultaneously the target and several comparison stars, allowing for effective removal of common instrumental and atmospheric systematics. We selected comparison stars less than 0.5 magnitude brighter and 1 magnitude fainter than HAT-P-23b and closest in  $B - V/J - K$  color space, following Rackham et al. (2017). We show the selected comparison stars in Table 1.

For ACCESS we have used several combinations of custom multi-slit masks, grisms, and blocking filters over time to refine our observations as the survey progresses. For the first transit of HAT-P-23b, in particular, we used  $20'' \times 12''$  wide slits for the science masks to adequately sample the sky background and narrower,  $20'' \times 0.5''$ , slits for the calibration masks to perform high precision wavelength calibration. We used the 150 lines/mm grism blazed at  $18.8^\circ$  (150-18.8) with the WB5600 blocking filter for this setup. We switched to a new field placement and a new science mask with wider  $90'' \times 10''$  slits for the last four transits to better sample the sky and get more uniform wavelength coverage. We used the 300 lines/mm grism blazed at  $17.5^\circ$  (300-17.5) with the GG495 blocking filter for the second through third transit, the 300 lines/mm grism blazed at  $17.5^\circ$  (300-17.5) with the GG455 blocking filter for the fourth transit, and the 300 lines/mm grism blazed at  $26.7^\circ$  (300-26.7) with the GG455 blocking filter for the fifth transit.

On average, these setups provide a resolving power of  $R \sim 1200$ , or approximately  $4.7 \text{ \AA}$  per resolution element, and access a full wavelength coverage of  $5,050 \text{ \AA}$ – $9,840 \text{ \AA}$ . In practice, the signal-to-noise ratio (SNR) blueward of  $\approx 5,400 \text{ \AA}$  and redward of  $\approx 9,300 \text{ \AA}$  dropped to roughly less than 25% of peak counts. For this reason, we omitted measurements outside of this range for the rest of the study. Finally, we omitted data taken during twilight and at airmasses of  $Z \geq 2$ , where large deviations in the white-light curve became apparent.

We summarize our observing configurations and conditions for each night in Table 2. We also note that the difference in wavelength coverage between nights comes from our choice to use wavelength ranges that maximized the integrated flux for a given night over uniformity in wavelength coverage. This might produce slight variations in the observed wavelength-binned transit depths, which can contribute to spurious slopes in the final transmission spectrum (McGruder et al. 2020). For HAT-P-23b, however, we recover a transmission spectrum with no typical activity-related slope (see Section 7), so this does not appear to be a significant effect in this case.

### 2.2. Data Collection

We observed the first transit (Transit 1) on 22 Jun 2016, the second (Transit 2) on 10 Jun 2017, the third (Transit 3) on 04 Jun 2018, the fourth (Transit 4) on 21 Jun 2018, and the fifth (Transit 5) on 22 Aug 2018. We used blocking filters for all nights to reduce contamination from light at higher orders, while also truncating the spectral range to  $5,300 \text{ \AA}$ – $9,200 \text{ \AA}$ . We made observations in Multi-Object Spectroscopy mode with  $2 \times 2$  binning in Fast readout mode (31 s) for all nights to take

**Table 1.** Target and comparison star magnitudes and coordinates from <https://vizier.u-strasbg.fr/viz-bin/VizieR?-source=I/322>.

Star	RA-J2000 (h:m:s)	Dec-J2000 (d:m:s)	B	V	J	K	D <sup>a</sup>
HAT-P-23	20:24:29.7	16:45:43.8	13.4	12.1	11.1	10.8	0.00
comp4	20:23:29.4	16:49:08.0	13.5	12.5	10.7	10.0	0.50
comp5	20:24:15.1	16:42:08.4	13.8	12.7	11.0	10.4	0.36

<sup>a</sup> $D \equiv \sqrt{[(B - V)_c - (B - V)_t]^2 + [(J - K)_c - (J - K)_t]^2}$ , where  $c$  and  $t$  refer to the given comparison star and HAT-P-23, respectively, in magnitudes.

**Table 2.** Observation log<sup>a</sup>

Transit	UT Date	Grism	BF	Mask (Cal, Sci)	Exp	SF	Airmass <sup>b</sup>
1	2016-06-22 06:13→10:03	150-18.8	WB5600	20 × 0.5, 20 × 12	15	300	1.5 → 1.4 → 2.2
2	2017-06-10 05:26→09:08	300-17.5	GG495	20 × 0.5, 90 × 10	50	165	1.9 → 1.4 → 1.5
3	2018-06-04 05:32→10:26	300-17.5	GG495	20 × 0.5, 90 × 10	30, 70	181	2.2 → 1.4 → 1.8
4	2018-06-21 05:14→10:03	300-17.5	GG455	20 × 0.5, 90 × 10	50, 70	172	1.7 → 1.4 → 2.1
5	2018-08-22 00:14→06:47	300-26.7	GG455	20 × 0.5, 90 × 10	70, 100	182	2.1 → 1.4 → 2.4

<sup>a</sup>**Abbreviations:** Blocking Filter (BF), Calibration (Cal) and science (Sci) mask slit dimensions in arcseconds, Exposure Time in seconds (Exp), Number of science frames (SF).

<sup>b</sup>The arrows indicate measurements taken at the beginning, middle, and end of the night.

advantage of the reduced readout noise. Depending on the instrument setup and seeing conditions, we adjusted the individual exposure times between 15–100 seconds to keep the number of counts per pixel between 30,000–49,000 counts (ADU; gain =  $1e^-$ /ADU on  $f/2$  camera), i.e., within the linearity limit of the CCD (Bixel et al. 2019).

With the calibration mask in place, we took a series of arcs using a HeNeAr lamp before each transit time-series observation. The narrower slit width of the calibration mask increased the spectral resolution of the wavelength calibration as well as avoided saturation of the CCD from the arc lamps. We took a sequence of high-SNR flats with a quartz lamp through the science mask to characterize the pixel-to-pixel variations in the CCD. As in our past studies (Rackham et al. 2017; Espinoza et al. 2019; Bixel et al. 2019; Weaver et al. 2020; McGruder et al. 2020), we did not apply a flat-field correction to the science images because it introduces additional noise in the data and does not improve the final results.

During the Transit 5 observation, the incorrect grism (300-26.7) was mistakenly inserted into the instrument in place of the intended 300-17.5 grism used in previous

nights. This led to the grism metadata stored in the header files to be incorrectly labelled as the 300-17.5 grism instead of 300-26.7, which we did not notice until after the data had been collected and the spectra examined and compared with previous data. The end result is data that are still usable, but slightly less dispersed relative to the other nights (1.25 Å/pixel vs. 1.341 Å/pixel), which we account for in the rest of our analysis. We show representative science frames from the CCD array in Figure 10 of the Appendix.

### 3. DATA REDUCTION AND LIGHT CURVE ANALYSIS

#### 3.1. Reduction pipeline

We reduced the raw data using the ACCESS pipeline described in previous ACCESS publications (Rackham et al. 2017; Espinoza et al. 2019; Bixel et al. 2019; Weaver et al. 2020; McGruder et al. 2020). The detailed functions of the pipeline, including standard bias and flat calibration, bad pixel and cosmic ray correction, sky subtraction, spectrum extraction, and wavelength calibration are described in Jordán et al. (2013) and Rackham et al. (2017). We briefly summarize the data reduction here.



We applied the wavelength solution found with the arc lamps to the first science image spectra and the remaining image spectra were then cross-correlated with the first image. We calibrated the spectra from all stars to the same reference frame by identifying shifts between the H $\alpha$  absorption line minimum of the median spectra and air wavelength of H $\alpha$ , and interpolated the spectra onto a common wavelength grid using b-splines. We aligned all spectra to within 2 Å, which is less than our average resolution element of 4.7 Å (see Section 2.1).

The final results of the pipeline are sets of wavelength-calibrated and extracted spectra for the target and each comparison star for each night as shown in Figure 1. We use those spectra to produce integrated white-light (Figure 11 in the Appendix) and spectrally binned light curves. The series of white-light curves produced in this fashion informed which comparison stars to omit in the rest of the analysis on a per transit basis, which we describe in Section 3.3.

### 3.2. Wavelength binning

For our main analysis, we used a set of semi-uniform bins with a main width of 200 Å, which we found to be a good compromise between spectral resolution and signal-to-noise considerations. In addition, we interspersed narrower bins centered around the air wavelength locations of Na I-D, K I, and Na I-8200 with widths of 185.80 Å, 54.00 Å, and 160.80 Å, respectively. We made the K I bin relatively narrow to avoid nearby tellurics. To check the results from our analysis based on this wavelength binning scheme, we separately used a set of 5 bins centered around each of these three species, set by the full width of their respective absorption lines (45 Å, 10 Å, and 40 Å). We share our two wavelength bin schemes in Tables 5 and 6 of the Appendix.

### 3.3. Comparison star selection

For each transit, we divided the white-light curve of HAT-P-23 by each of the comparison stars common to each night (comp4 and comp5) to select which data points to use for each night (Figure 11). For a given comparison star, we defined fluxes more than  $2\sigma$  apart from adjacent points in the divided white-light curve to be potential outliers for that night, where  $1\sigma$  was defined to be the photometric noise for that night. Because this set could contain false-positives caused by an actual non-outlying point surrounded by two positive outliers, we then manually went back and removed these types of points from the potential set of outliers. Conversely, we also manually included false-negatives in the outlier set. These were points not initially marked as outliers because they were part of an overall feature, for example

the large decrease in flux. Finally, we omitted the union of these selected outliers from all nights from the rest of our analysis. With this set of selected data points and comparison stars for each transit epoch, we next performed the detrending of the resulting light curves as described in Section 4.

## 4. DETRENDING ANALYSIS

### 4.1. Methodology overview

We used Gaussian Process (GP) regression techniques combined with principle component analysis (PCA) to detrend our reduced data, following (Espinoza et al. 2019). GPs are a flexible and robust tool for modeling data in the machine learning community (Rasmussen & Williams 2005) that has gained popularity in the exoplanets field (see, e.g., Gibson et al. 2012, Aigrain et al. 2012). Gibson et al. (2012) provides a good overview to this methodology applied to exoplanet transit light curves. Applying this methodology for a collection of  $N$  measurements ( $\mathbf{f}$ ), such as the flux of a star measured over a time series, the log marginal likelihood of the data can be written as:

$$\log \mathcal{L}(\mathbf{r}|\mathbf{X}, \boldsymbol{\theta}, \boldsymbol{\phi}) = -\frac{1}{2} \mathbf{r}^\top \boldsymbol{\Sigma}^{-1} \mathbf{r} - \frac{1}{2} \log |\boldsymbol{\Sigma}| \quad (1)$$

$$- \frac{N}{2} \log(2\pi) \quad , \quad (2)$$

where  $\mathbf{r} \equiv \mathbf{f} - T(\mathbf{t}, \boldsymbol{\phi})$  is the vector of residuals between the data and analytic transit function  $T$ ;  $\mathbf{X}$  is the  $N \times K$  matrix for  $K$  additional parameters, where each row is the vector of measurements  $\mathbf{x}_n = (x_{n,1}, \dots, x_{n,K})$  at a given time  $n$ ;  $\boldsymbol{\theta}$  are the hyperparameters of the GP;  $\boldsymbol{\phi}$  are the transit model parameters; and  $\boldsymbol{\Sigma}$  is the covariance of the joint probability distribution of the set of observations  $\mathbf{f}$ . In our analysis, we used six systematics parameters: time, full width at half maximum (FWHM) of the spectra on the CCD, airmass, position of the pixel trace through each spectrum on the chip of the CCD, sky flux, and shift in wavelength space of the trace.

We used the Python package `batman` (Kreidberg 2015) to generate our analytic transit model. We used the open-source package `ld-exosim`<sup>7</sup> (Espinoza & Jordán 2016) to identify the appropriate limb-darkening law for this model, which we found to be the logarithmic law. From here, the log posterior distribution  $\log \mathcal{P}(\boldsymbol{\theta}, \boldsymbol{\phi}|\mathbf{f}, \mathbf{X})$  can be determined by placing explicit priors on the maximum covariance hyperparameters and the scale length hyperparameters. From  $\mathcal{P}$ , the transit parameters can then be inferred by optimizing with respect to  $\boldsymbol{\theta}$  and  $\boldsymbol{\phi}$ .

<sup>7</sup><https://github.com/nespinoza/ld-exosim>

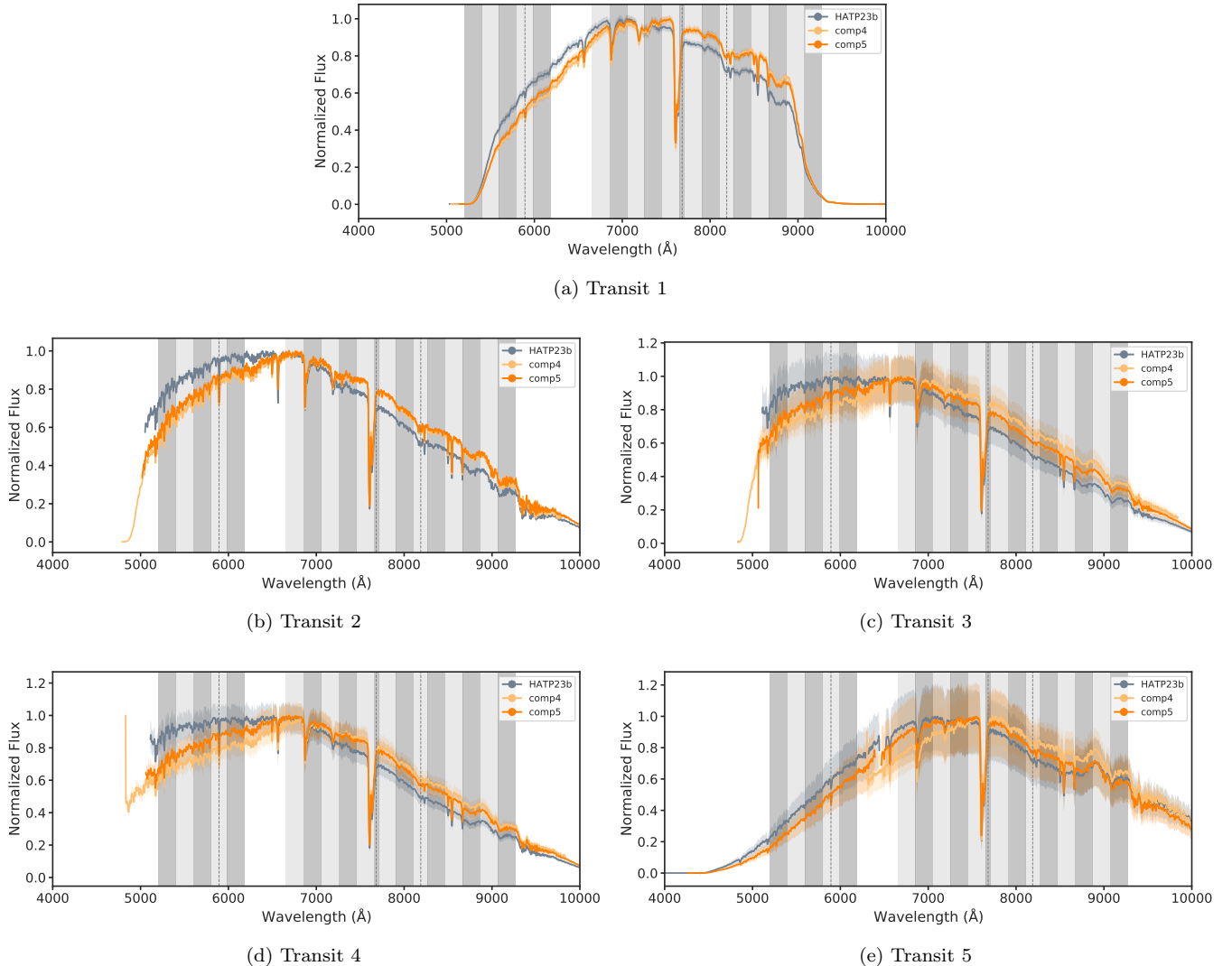


**Figure 1.** Optimally extracted spectra over the course of each night for each star. The median (solid line) and  $1\sigma$  region region are shown for the target and each comparison star used, along with the wavelength bin scheme used. We note that the first and last bin needed to be omitted for Transit 1 due to lack of flux. The gap in bins is due to the chip gap introduced in Transit 5. (</>)

#### 4.2. Sampling methodology

We accomplished the above optimization problem with the Bayesian inference tool, `PyMultiNest` (Buchner et al. 2014), using 1000 live points and computed the log likelihoods from the GP with the `george` (Ambikasaran et al. 2015) package. We implemented this detrending scheme by simultaneously fitting the data with a Matérn-3/2 kernel for the GP under the assumption that points closer to each other are more correlated than points farther apart. The PCA methodology follows from Jordán et al. (2013) and Espinoza et al. (2019), where  $M$  signals,  $S_i(t)$ , can be extracted from  $M$  comparison stars and linearly reconstructed according to the eigenvalues,  $\lambda_i$ , of each signal. This allows for the optimal extraction of informa-

tion from each comparison star to inform how the total flux of HAT-P-23 varies over the course of the night.

#### 4.3. Parameterization improvements

In past work, we depended on the ratio of the semi-major axis to stellar radius ( $a/R_s$ ) as an input transit parameter. With *Gaia*, we are now able to invert the problem by using the newly determined measurements of the stellar density ( $\rho_s$ ) from *Gaia* Data Release 2 (Gaia Collaboration et al. 2018) to place tighter constraints on  $a/R_s$ . Applying our standard assumption of a circular Keplerian orbit with period  $P$  then yields  $a/R_s = [(GP^2)/(3\pi)]^{1/3} \rho_s^{1/3}$ , where  $G$  is the gravitational constant. In addition, we implemented the technique introduced by Espinoza (2018) for reparam-

terizing the impact parameter ( $b$ ) and planet-to-stellar radius ratio ( $p \equiv R_p/R_s$ ) to further improve our transit parameter sampling. In this technique, these transit parameters are expressed as functions of the random variables  $r_1 \sim U(0, 1)$  and  $r_2 \sim U(0, 1)$ , and efficiently sampled from a region bounded by the physical constraints of transiting systems (i.e.  $0 < b < 1 + p$ ). This is a natural analog to the uniform sampling method of limb darkening coefficients introduced in [Kipping \(2013\)](#).

#### 4.4. Transmission spectrum construction

Finally, we Bayesian model averaged the principal components together, which we determined by detrending with one, then two, up to  $M$  principal components, to create the final detrended white-light curves and model parameters of interest. We present the resulting white-light curves in [Figure 2](#), the best-fit parameters in [Table 3](#), and associated corner plots in [Figure 12](#) of the Appendix. To create the transmission spectrum for each night ([Figure 4](#)), we applied the same detrending methodology to the wavelength-binned light curves (described in [Section 3.2](#)), keeping all transit parameters fixed to the fitted white-light curve values except for the transit depth and limb darkening parameters. Because the impact parameter needed to be held fixed for the binned fitting, we sampled directly for it instead of uniformly sampling in  $(b, p)$  space. We used a truncated normal distribution for this sampling, given by:

$$\xi = \frac{x - \mu}{\sigma}, \quad \alpha = \frac{a - \mu}{\sigma}, \quad \beta = \frac{b - \mu}{\sigma} \quad (3)$$

$$Z = \Phi(\beta) - \Phi(\alpha) \quad , \quad (4)$$

where  $x$  is the binned planet-to-star radius ratio,  $\mu$  is the mean fitted white-light curve depth,  $\sigma$  is the corresponding  $1\sigma$  uncertainty on that depth,  $a = 0$ ,  $b = 1$ , and  $\Phi(\cdot)$  is the cumulative distribution function.

## 5. STELLAR ACTIVITY

Before combining the transmission spectra from each night, we first considered the impact of stellar photospheric heterogeneity, which can have an observable effect on transmission spectra ([Pont et al. 2008, 2013](#); [Sing et al. 2011](#); [Oshagh et al. 2014](#); [Zhang et al. 2018](#)), even if magnetically active regions are not occulted by the transiting exoplanet ([McCullough et al. 2014](#); [Rackham et al. 2018, 2019](#); [Apai et al. 2018](#)). Qualitatively, global variations in stellar activity could manifest themselves as an overall dimming or brightening of the star, which could lead to significant variations in transit depths. Changes in photometric activity can roughly correlate with the covering fraction of starspots, which in turn can modulate the luminosity of the star and impact observed transit depths

([Berta et al. 2011](#)), although [Rackham et al. \(2019\)](#) show that this relationship is very non-linear. Those variations can also be wavelength-dependent, leading to slopes with spurious spectral features in the transmission spectrum.

To assess the brightness variations of HAT-P-23 over the time frame of our observations, we used 2015 Aug 12 – 2018 Oct 17 photometric observations from 566 out-of-transit V-band images of HAT-P-23 taken by Ohio State University’s All-Sky Automated Survey for Supernovae<sup>8</sup> (ASAS-SN) program ([Shappee et al. 2014](#); [Kochanek et al. 2017](#)).

The ASAS-SN photometry is sampled much more coarsely than our transit observations, so we again used a GP routine ([Carter et al. 2020](#); [Weaver et al. 2020](#); [Alam et al. 2018](#)) to model quasi-periodic modulations in the data and estimate the amplitude of the photometric variation induced by stellar activity during each of the five transit epochs of HAT-P-23. Following [Alam et al. \(2018\)](#), we used a negative log likelihood kernel along with a gradient-based optimization routine to find the best-fit hyperparameters, assuming a stellar rotation period  $P_{\text{rot}} = 7$  days from [Schrijver \(2020\)](#). [Figure 3](#) shows the GP regression model for the relevant ASAS-SN data. Overall, the relative flux from the photometric monitoring model varied by as much as 2% from the median value obtained from the GP. Although the ASAS-SN observations are too coarse to effectively sample the photometric activity during times of transits, this data still gives us valuable insight into the variations in stellar flux between epochs.

The white-light transit depths ([Table 3](#)) between these epochs varied by as much as 600 ppm ( $\approx 5\%$ ) from the weighted-mean white-light curve depth (12,966 ppm  $\pm$  228 ppm), an effect that can be attributed to the observed stellar variability, differences in the relative spectral flux of the comparison stars used, or differences in wavelength coverage introduced by chip gaps ([McGruder et al. 2020](#)).

We find that, in this case, changes in stellar disk coverage by unocculted heterogeneities likely drive the white-light curve depth variations that we observe between transit epochs of HAT-P-23b. For example, assuming that unocculted starspots effectively radiate as a single black body with temperature  $T_{\text{sp}}$ , the required covering fraction  $f_{\text{sp}}$  needed to produce the observed change in luminosity ( $\Delta L_{\text{obs}} \equiv L_{\text{obs,sp}}/L_{\text{obs,0}}$ ) would be:

$$f_{\text{sp}} = \frac{T_0^4}{T_0^4 - T_{\text{sp}}^4} (1 - \Delta L_{\text{obs}}) \quad , \quad (5)$$

<sup>8</sup><https://asas-sn.osu.edu>

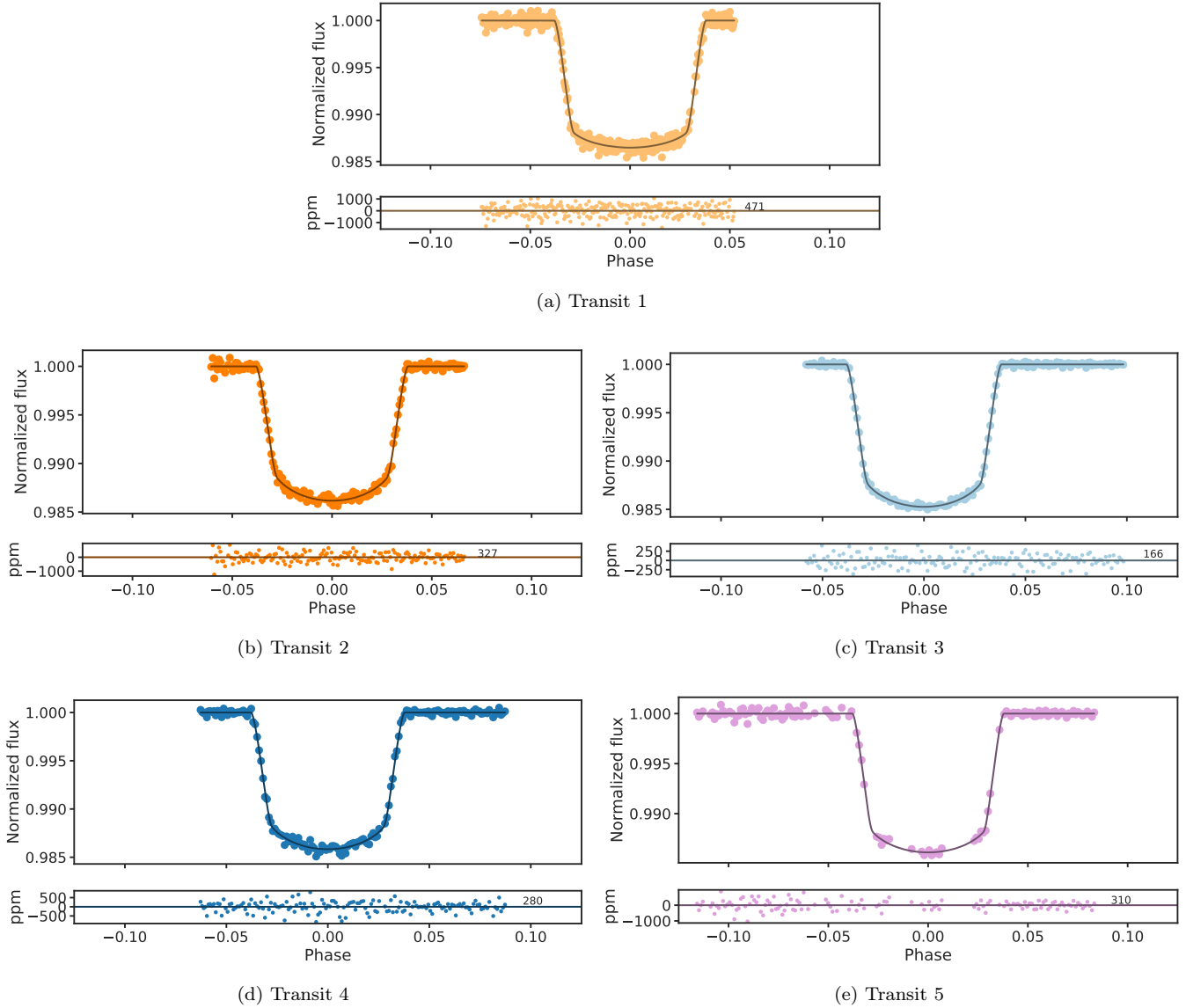


**Figure 2.** Detrended white-light curves for each night used in our final analysis. The white-light curves are shown for the maximum number of principal components used (2). We share the model-averaged transit parameters in Table 3 and associated corner plots in Figure 12 of the Appendix. (</>)

where  $T_0$  is the effective temperature of HAT-P-23,  $L_{\text{obs,sp}}$  is its observed luminosity in the presence of the spot, and  $L_{\text{obs},0}$  is the observed luminosity assuming an immaculate photosphere. Because we take this as a ratio, it is equivalent to using the observed flux. Using the minimum relative flux and median relative flux estimated from our GP analysis in Figure 3 for this ratio ( $\approx 0.92$  and  $0.94$ , respectively), the effective temperature of HAT-P-23b ( $T_0 \approx 5,900$  K), and temperatures for the spot  $T_{\text{sp}} \approx 2,200$  K– $3,800$  K (we justify this choice of temperatures in Section 7), we estimate spot covering fractions ranging from  $\approx 2.2\%$ – $2.6\%$ . For this reason, we calculate and apply transit depth offset corrections as

described in Section 6 before building the final transmission spectrum. In Section 7 we model the contribution of an unocculted heterogeneous photosphere to the resulting transmission spectrum, informed by the photometric monitoring data.

## 6. TRANSMISSION SPECTRUM

### 6.1. Combining nights

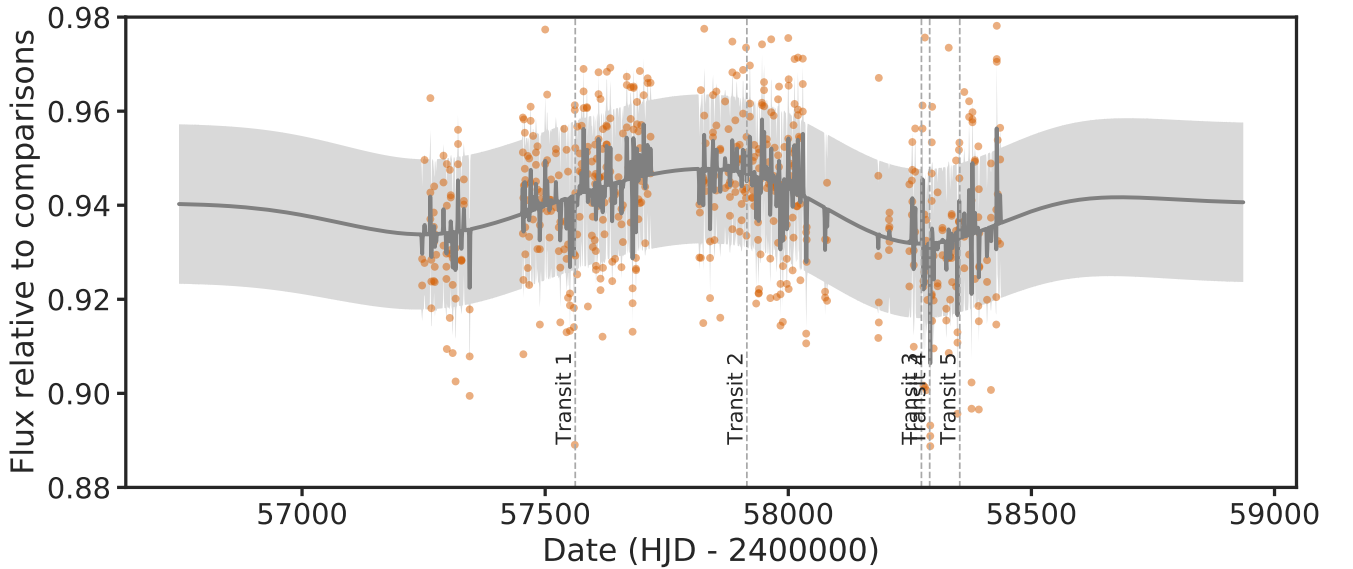
The uncertainties in the wavelength-binned transit depths from our individual transits (Table 7) range from 208 ppm–1,445 ppm, which is not precise enough to detect the atmosphere of HAT-P-23b. For example, a hydrogen-dominated composition for the atmosphere of



**Table 3.** Fitted model averaged transit parameters from GP+PCA detrending method shown in Figure 2. We share the associated corner plots in Figure 12 of the Appendix.

parameter <sup>a</sup>	Transit 1	Transit 2	Transit 3	Transit 4	Transit 5
$\delta$	$12584.79890^{+633.98979}_{-647.93827}$	$12716.26467^{+421.08962}_{-459.31331}$	$13571.18577^{+598.68259}_{-650.42694}$	$13204.48610^{+472.94430}_{-465.37117}$	$12831.57340^{+456.65963}_{-489.88214}$
$R_p/R_s$	$0.11218^{+0.00283}_{-0.00289}$	$0.11277^{+0.00187}_{-0.00204}$	$0.11650^{+0.00257}_{-0.00279}$	$0.11491^{+0.00206}_{-0.00202}$	$0.11328^{+0.00202}_{-0.00216}$
$t_0$	$4852.26537^{+0.00015}_{-0.00015}$	$4852.26540^{+0.00014}_{-0.00014}$	$4852.26541^{+0.00014}_{-0.00013}$	$4852.26545^{+0.00015}_{-0.00015}$	$4852.26543^{+0.00013}_{-0.00014}$
$P$	$1.21289^{+1.13e-07}_{-1.14e-07}$	$1.21289^{+8.45e-08}_{-8.76e-08}$	$1.21289^{+8.76e-08}_{-8.78e-08}$	$1.21289^{+7.42e-08}_{-7.84e-08}$	$1.21289^{+7.00e-08}_{-7.13e-08}$
$\rho_s$	$1.07230^{+0.08406}_{-0.07603}$	$0.96894^{+0.06463}_{-0.05683}$	$1.01504^{+0.05602}_{-0.05063}$	$1.03666^{+0.06581}_{-0.06079}$	$1.02626^{+0.07229}_{-0.07204}$
$i$	$84.33384^{+0.88921}_{-0.80101}$	$83.14471^{+0.73406}_{-0.61691}$	$83.64261^{+0.56957}_{-0.51338}$	$83.76319^{+0.69346}_{-0.64068}$	$83.73923^{+0.73109}_{-0.74358}$
$b$	$0.43173^{+0.04848}_{-0.05892}$	$0.50417^{+0.03445}_{-0.04412}$	$0.47517^{+0.02969}_{-0.03537}$	$0.46904^{+0.03843}_{-0.04320}$	$0.46936^{+0.04278}_{-0.04503}$
$a/R_s$	$4.36890^{+0.11130}_{-0.10580}$	$4.22377^{+0.09190}_{-0.08424}$	$4.28971^{+0.07750}_{-0.07254}$	$4.31996^{+0.08955}_{-0.08614}$	$4.30547^{+0.09880}_{-0.10320}$
$u$	$0.24859^{+0.10290}_{-0.10754}$	$0.38699^{+0.07698}_{-0.07472}$	$0.37032^{+0.10186}_{-0.11732}$	$0.40126^{+0.08643}_{-0.09298}$	$0.32686^{+0.07151}_{-0.08796}$

<sup>a</sup>Parameter definitions:  $\delta = (R_p/R_s)^2$  - transit depth (ppm),  $R_p/R_s$  - planet radius / stellar radius,  $t_0$  mid-transit time (JD - 245000),  $P$  - period (days),  $\rho_s$  - stellar density (g/cc),  $i$  - inclination (degrees),  $b$  - impact parameter,  $a/R_s$  - semi-major axis / stellar radius,  $u$  - linear limb darkening coefficient.

**Figure 3.** Ground-based photometric observations of HAT-P-23 from ASAS-SN (points) during each transit epoch (dashed vertical lines). The flux is relative to the average brightness of the comparison stars used in this survey. The Gaussian process regression model (solid line) and  $1\sigma$  uncertainty (shaded region) fit to ASAS-SN data are also overplotted. (</>)

HAT-P-23b would produce a signal  $\Delta D$  of 384 ppm at 5 scale heights (based on eq. 11 of Miller-Ricci et al. 2009, using the most up to date system parameters from the literature shared in Section 1). Therefore, we needed to combine the transmission spectra from the five transits to be sensitive to atmospheric features of the planet.

We offset each transmission spectrum by the difference in its white-light curve depth from the weighted mean white-light curve depth for all nights and then average the offset transmission spectra together, weighted by the wavelength-dependent uncertainty estimated from the

wavelength-binned fitting. We combined the asymmetrical uncertainties according to Model 1 of Barlow (2003) and present the final results in Figure 4.

To verify our methodology, we also repeated our analysis up to this point using the wavelength binning scheme described in Section 3.2 that is centered around Na I-D, K I, and Na I-8200. The resulting combined transmission spectrum (Figure 5) shows no excess absorption near the species we examined, in agreement with our retrieval analysis discussed in Section 7.

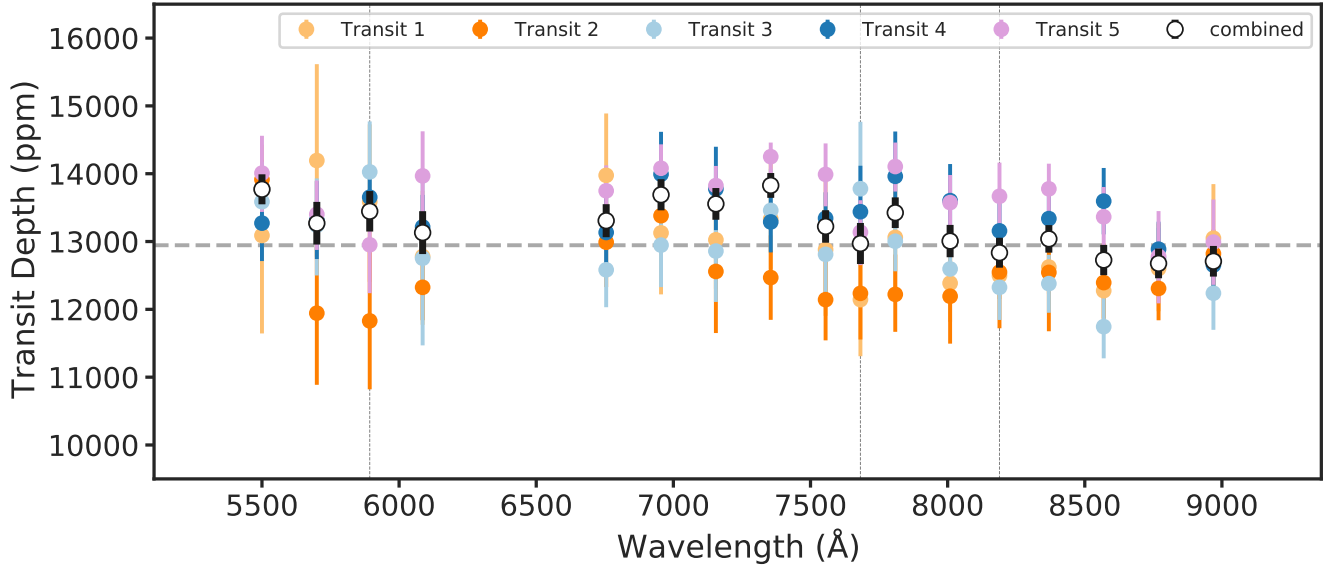


**Figure 4.** Transmission spectrum built from binned light curves show in Figures 13 – 17. From left to right, the vertical dashed lines mark the air wavelength locations of Na I -D, K I, and Na I -8200, respectively. For reference, the weighted mean white-light curve depth of 12,966 ppm is shown by the horizontal dashed line. The tabulated data for the above transmission spectra are available in Table 7 of the Appendix. (</>)

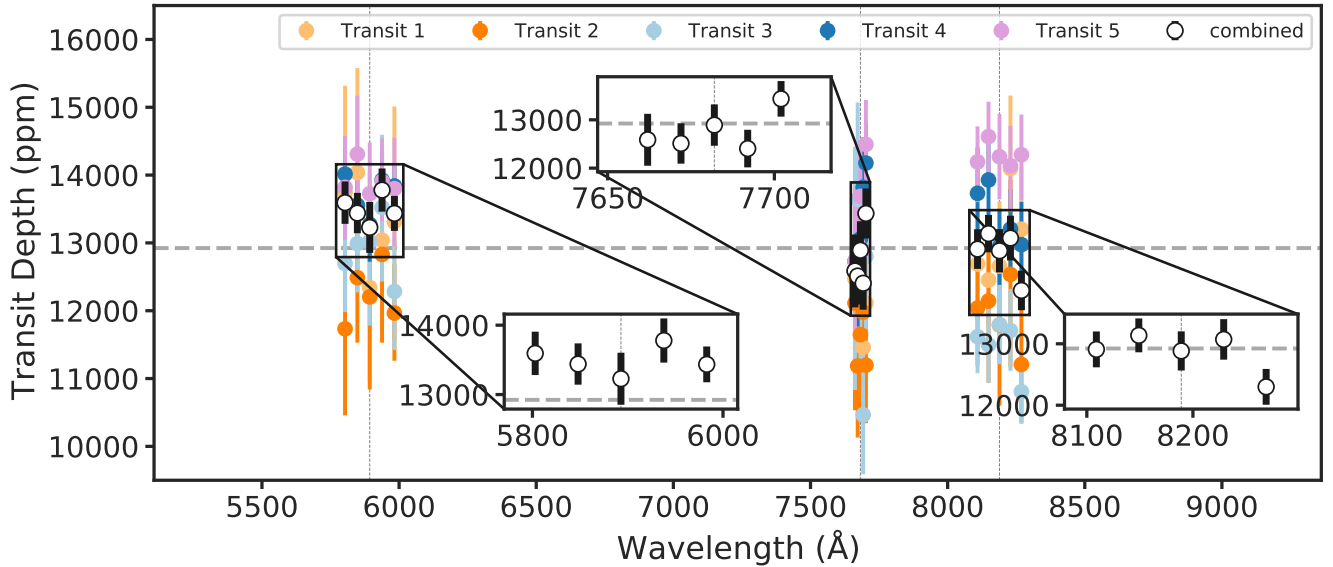


**Figure 5.** Same as Figure 4, but for wavelength bins centered around the above species and with a resulting weighted mean transit depth of 12,948 ppm. We observe no excess absorption near any of the species investigated. The tabulated data for the above transmission spectra are available in Table 8 of the Appendix. (</>)

## 7. ATMOSPHERIC MODELING

We employed both forward modeling and retrieval modeling techniques to interpret our combined transmission spectrum. Initial retrieval analysis with our custom code `exoretreats` (Bixel et al. 2019; Espinoza et al. 2019; Weaver et al. 2020; McGruder et al. 2020) favored models including stellar heterogeneity, but with the caveat that the corresponding spot covering fractions needed to take

up nearly a third of the star’s surface area. From our analysis of the ASAS-SN photometric light curve of HAT-P-23, shown in section 5, we estimate an average spot coverage fraction of about 2.2% to 2.6% of the surface of the star, so the result of the retrievals seems unphysical. We next turned to the one-dimensional radiative-convective-chemical equilibrium model ATMO (Goyal et al. 2018) to examine our spectrum, omitting contributions

from stellar activity. This analysis (described in Section 7.1) favored a transmission spectrum containing TiO/VO, which then informed our next step.

Given that TiO/VO can originate from spots with temperatures similar to M type stars, we returned to retrievals to investigate if this signal persisted after taking stellar activity into account. To address the previous problem with the retrievals (i.e. fitting freely spot contamination introduced too many degrees of freedom, yielding to best fits with unphysical spot properties), we assumed spot models instead, with the spot parameter values derived in Section 5.

Assuming that this signal in the transmission spectrum comes from spots on HAT-P-23, we bound our retrievals to spot temperatures where TiO is stable in sun-like stars ( $T_{\text{sp,lower}} = 2,200 \text{ K}$ ,  $T_{\text{sp,upper}} = 3,800 \text{ K}$ ), setting the lower and upper bound on the corresponding spot covering fractions estimated in Equation 5 to ( $f_{\text{sp,lower}} = 0.022$ ,  $f_{\text{sp,upper}} = 0.026$ ), respectively. We discuss the results of making this assumption in Section 7.2.

### 7.1. Forward modeling analysis

We used a generic grid of forward model transmission spectra as detailed in Goyal et al. (2019) to interpret the observations of HAT-P-23b. This grid of models has been generated using the 1D-2D radiative-convective equilibrium model ATMO (Tremblin et al. 2015; Amundsen et al. 2014; Drummond et al. 2016; Goyal et al. 2018). The model transmission spectra in the grid are generated for a Jupiter-like (radius and mass) planet around a Sun-like star. However, this can be scaled to any hot Jupiter exoplanet with H<sub>2</sub>-He dominated atmosphere using a scaling relationship detailed in Goyal et al. (2019). Each model in the grid assumes chemical equilibrium abundances and isothermal pressure-temperature (P-T) profiles. The model spectra includes H<sub>2</sub>-H<sub>2</sub>, H<sub>2</sub>-He collision-induced absorption (CIA) and opacities due to H<sub>2</sub>O, CO<sub>2</sub>, CO, CH<sub>4</sub>, NH<sub>3</sub>, Na, K, Li, Rb, Cs, TiO, VO, FeH, PH<sub>3</sub>, H<sub>2</sub>S, HCN, SO<sub>2</sub> and C<sub>2</sub>H<sub>2</sub>. The entire grid spans 24 equilibrium temperatures from 300 K–2,600 K in steps of 100 K, six metallicities (0.1–200x solar), four planetary gravities (5 m/s<sup>2</sup>–50 m/s<sup>2</sup>), four C/O ratios (0.35)–1.0), two condensation regimes (local and rainout condensation) and four parameters each describing scattering hazes and uniform clouds. The haze parameter is defined as the multiplicative factor to the wavelength dependent Rayleigh scattering due to small particles, whilst the cloud parameter is defined as the multiplicative factor to uniform grey scattering, simulating the effects of a cloud deck, where a factor of 0 indicates no clouds, while a factor of 1 indicates extremely cloudy. Further details can be found in Goyal et al. (2019).

#### 7.1.1. Forward model results and interpretation

The best-fit forward model is found by scaling each model in the grid to the parameters of HAT-P-23b and finding the model with the lowest  $\chi^2$  throughout the entire grid. Figure 6 shows this best-fit forward model spectrum with the  $\chi^2$  value of 34.25 and reduced  $\chi^2$  value of 2.14 with 16 degrees of freedom (17 data points minus 1). We also note that while fitting the forward model grid to the observed spectrum, a wavelength-independent constant vertical offset (transit depth) between model and observed spectra is a free parameter. The best-fit model is consistent with a temperature of 2500 K, ten times solar metallicity, and C/O ratio of 0.35, without any haze or clouds. For both the condensation regimes (local and rainout), we find the best-fit model is the same, which is driven by the very high best-fit temperature (2500 K), where rarely any condensation occurs. Figure 18 shows the  $\chi^2$  map of all the models in the grid when fitted to observations, along with contours of confidence intervals. There is a clear preference for high-temperature models. There is also a preference for low C/O ratio models within one sigma, due to lack of spectral features of any carbon-based species. However, the other parameters are less constrained. The rise in the transit depth that begins after 4,000 Å in this model spectrum is due to TiO/VO opacity. Thus the best-fit forward model for HAT-P-23b hints towards the presence of TiO/VO in its atmospheric limb.

### 7.2. Retrieval analysis

With this key insight from our forward modeling analysis, we next performed a retrieval analysis with exoretrievals similar to the one described in Weaver et al. (2020), with the key difference being now holding the spot parameters fixed to values informed from the host star’s photometry. We explored a suite of models for the bounding spot parameters ( $T_{\text{sp,lower}}, f_{\text{sp,lower}} = (2,200 \text{ K}, 0.022)$ ) and ( $T_{\text{sp,upper}}, f_{\text{sp,upper}} = (3,800 \text{ K}, 0.026)$ ), and atmospheric models including Na I, K I, and TiO, and assuming: i) a clear atmosphere (clear), ii) an atmosphere with clouds (clear+cloud), iii) an atmosphere with hazes (clear+haze), and a clear atmosphere in the presence of a starspot (clear+spot).

We ran these various models both fitting for the mean reference radius,  $R_0$ , and leaving it fixed to our weighted mean white-light value (using the  $R_p/R_s$  values in Table 3), to investigate its degeneracy with clouds. All models used the updated value for the stellar radius ( $R_s = 1.152 R_s$ ) from Stassun et al. (2019). In total, we explored 224 possible retrievals: 8 combinations of the model types (clear, cloud, haze, spot)  $\times$  7 combinations

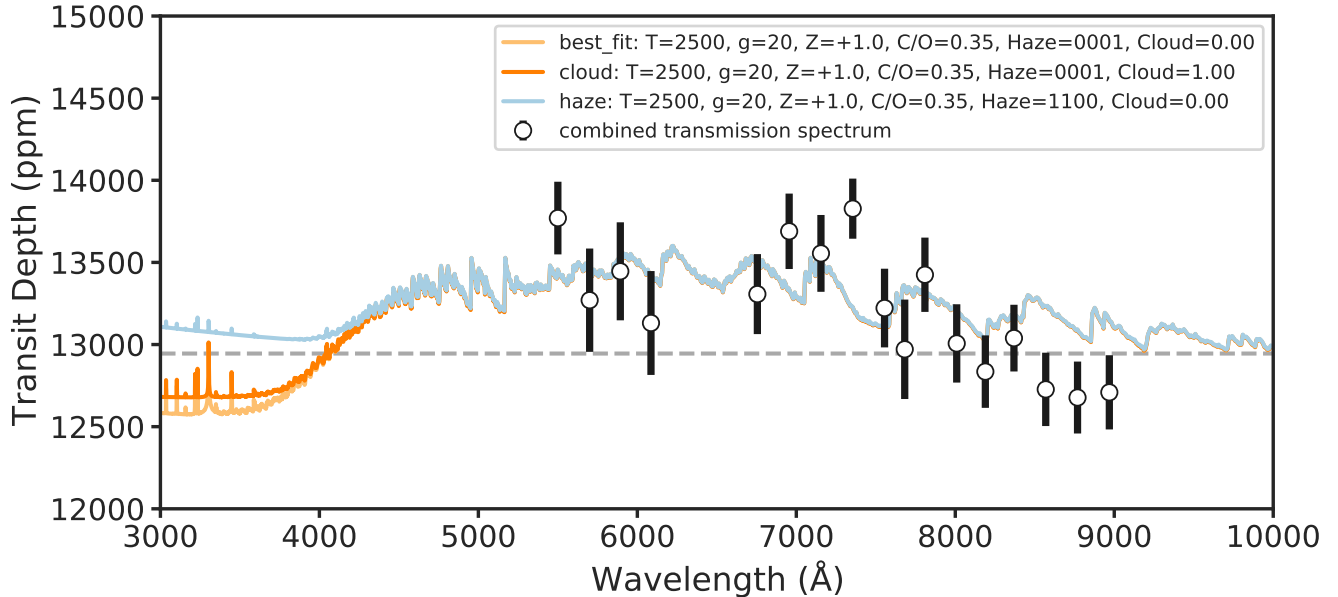


**Figure 6.** Final combined transmission spectrum from Figure 4 (filled white circles) compared to a best-fit (yellow), cloud (orange), and haze (blue) model found from forward modeling on a generic grid. The weighted mean white-light curve depth is also shown here (grey dashed line) for comparison. We share the  $\chi^2$  map of the entire grid in Figure 18 of the Appendix. (</>)

of the three species  $\times$  4 combinations of the fixed spot temperatures/covering fractions with and without fitting for  $R_0$ .

### 7.3. Retrieval results and interpretations

The suite of retrieval models described above all returned consistent results marginally favoring TiO being present in the atmosphere of HAT-P-23b, with the most favored model corresponding to a sub-solar to super-solar TiO abundance of  $10^{-7.1 \pm 4}$ . We share a representative summary of the Bayesian log-evidence of each model relative to the model with the lowest log-evidence in Figure 7 and associated priors in Table 4. We also show a selection of the retrieved transmission spectra in Figure 8, and the summary statistics for the corresponding posterior distributions in Table 9 of the Appendix.

Although models including TiO in the atmosphere of the planet without contributions from stellar activity tended to be preferred in all retrieval combinations examined, the preference over stellar activity was not as large when fitting for  $R_0$  (Figure 7, right panel). For that case, the log-evidence for every model was below 5, making the differences between specific models less statistically significant. New data collected in the UV and IR would allow for more robust retrieval results in this case. Finally, we note that because these retrievals are a 1D analysis, our retrieved terminator planet temperatures are consistently cooler than the expected equilibrium temperature of HAT-P-23b, as predicted by MacDonald et al. (2020); Pluriel et al. (2020).

### 7.4. Implications and broader context

The trend between exoplanets with known surface gravity and equilibrium temperature vs. water feature strength in the near-IR, proposed by Stevenson (2016), would predict that HAT-P-23b has a clear atmosphere. In the re-analysis of this relationship by Alam et al. (2020) using new data from the Hubble Space Telescope’s Wide Field Camera 3 (*HST/WFC3*) (Wakeford et al. 2019), they note that this divide may not be as distinct as initially suggested. Because of its high surface gravity ( $g \approx 30 \text{ m/s}^2$ ) and relatively high equilibrium temperature ( $T_{eq} = 2,027 \text{ K}$ ), HAT-P-23b tests a region of parameter space previously unexplored (see Figure 9). Measurements of its transmission spectrum in the *J*-band ( $1.36 \mu\text{m}$ – $1.44 \mu\text{m}$ ) and baseline region ( $1.22 \mu\text{m}$ – $1.30 \mu\text{m}$ ) to determine the planet’s water feature signal would provide insight into this potential trend in exoplanet atmosphere types. For example, a single transit in the  $7,500 \text{ Å}$ – $18,000 \text{ Å}$  IR range with G141 grism aboard *HST/WFC3* would provide the novel data needed for such an analysis. In addition, a second transit in the UV/Visible channel with the  $2,000 \text{ Å}$ – $8,000 \text{ Å}$  grism (G280) (Wakeford et al. 2020) would provide the wide wavelength coverage necessary to perform a robust retrieval of the combined transmission spectrum and test our preliminary result.

## 8. SUMMARY AND CONCLUSIONS

We collected, extracted, and combined transmission spectra of HAT-P-23b from *Magellan/IMACS* from five

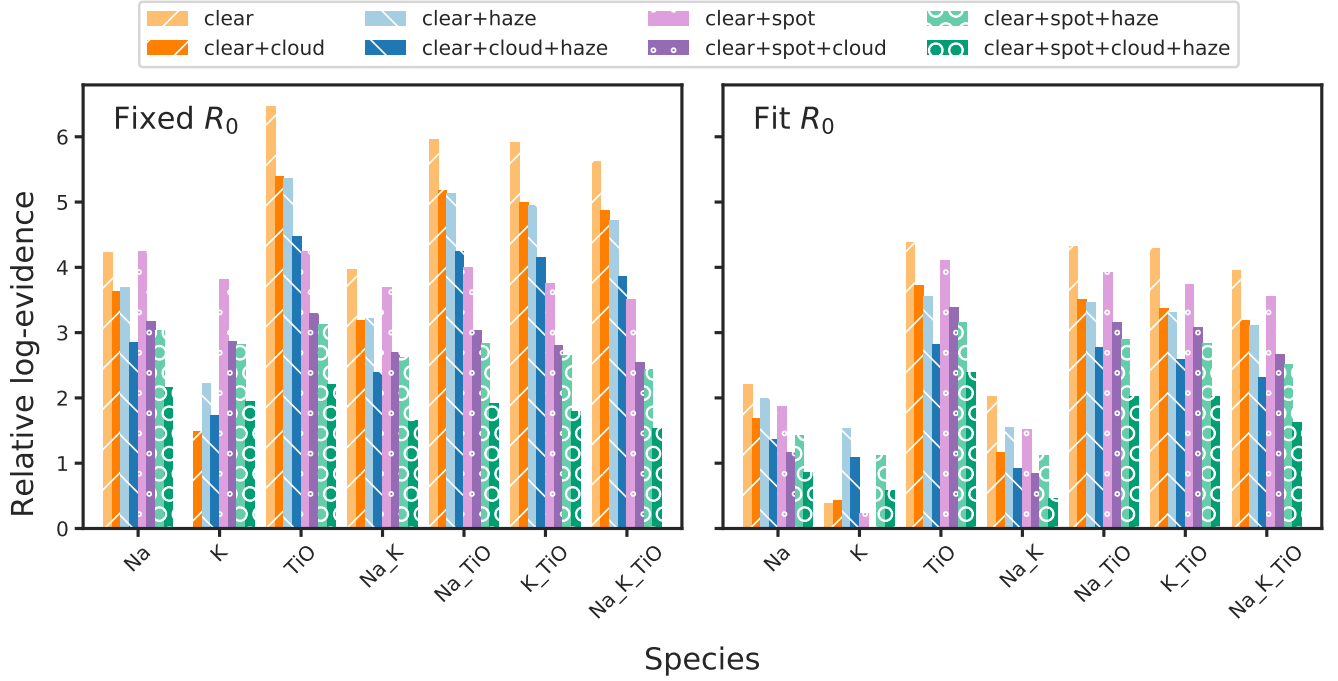


**Figure 7.** Representative summary of Bayesian log-evidences of retrieved models relative to the model with the lowest log-evidence (left: Fixed  $R_0$ , K, clear; right: Fit  $R_0$ , K, clear+spot+cloud). Both sets correspond to  $(T_{\text{sp,lower}}, f_{\text{sp,lower}}) = (2,200 \text{ K}, 0.022)$ , with  $R_0 = 12,966 \text{ ppm}$  fixed to our observed mean white-light curve depth in the left panel. A trend can be seen favoring models with TiO present in the planet’s atmosphere over contributions originating from stellar activity. ([⟨/⟩](#))

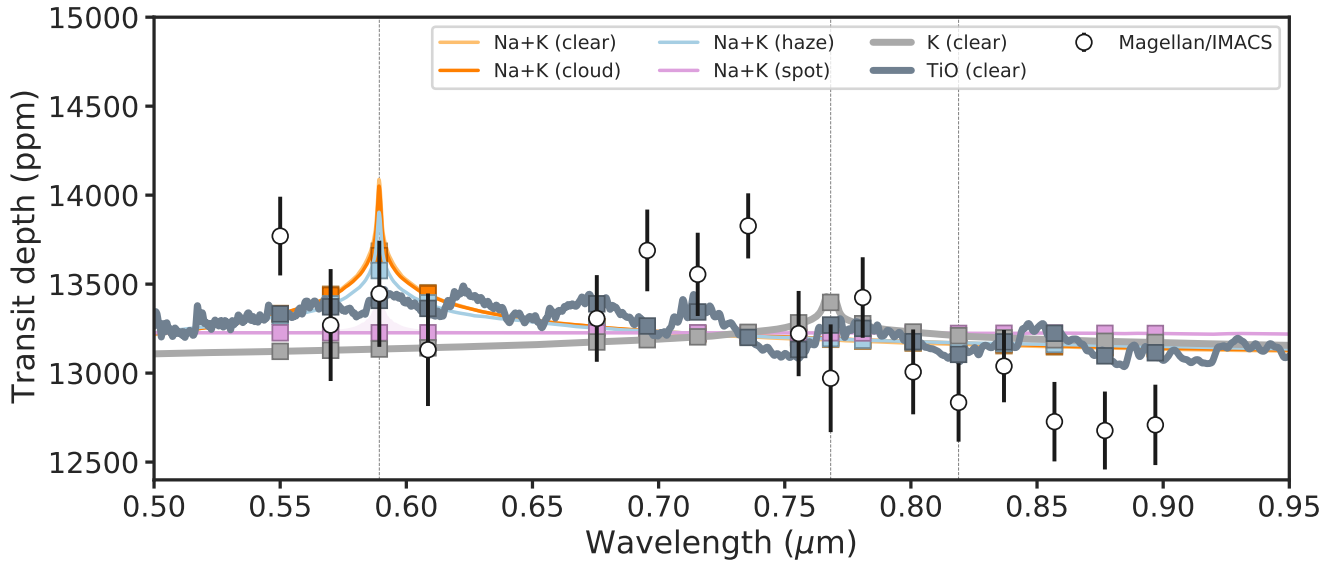


**Figure 8.** Sample retrieved transmission spectra demonstrating the impact of different retrieval models on the overall shape of the spectrum when  $R_0$  is held fixed (Figure 7, left panel). We also include the models with the lowest (K, clear) and highest (TiO, clear) log-evidence in bold for comparison. Other models including TiO were omitted because of their visual similarity. We included the associated retrieved parameters for each model in Table 9 of the Appendix. ([⟨/⟩](#))



**Table 4.** Priors used to produce Figures 7 and 8.

Parameter	Definition	Prior (uniform)
$f$	reference planet radius normalization ( $fR_0$ )	[0.8, 1.2]
$\log P_0$	log10 cloud top pressure (bar)	[-6, 6]
$T_p$	planet atmospheric temperature (K)	[100, 3000]
$\log(\text{species})$	trace species mixing ratio	[-30, 0]
$\log \sigma_{\text{cloud}}$	log10 grey opacity cross section	[-50, 0]
$\log a$	log10 haze amplitude	[-30, 30]
$\gamma_{\text{haze}}$	haze power-law	[-4, 0]
$T_{\text{star}}$	occulted stellar temperature (K)	[5420, 6420]
$T_{\text{het}}$	star spot temperature (K)	[2200]
$f_{\text{het}}$	spot covering fraction	[0.022]

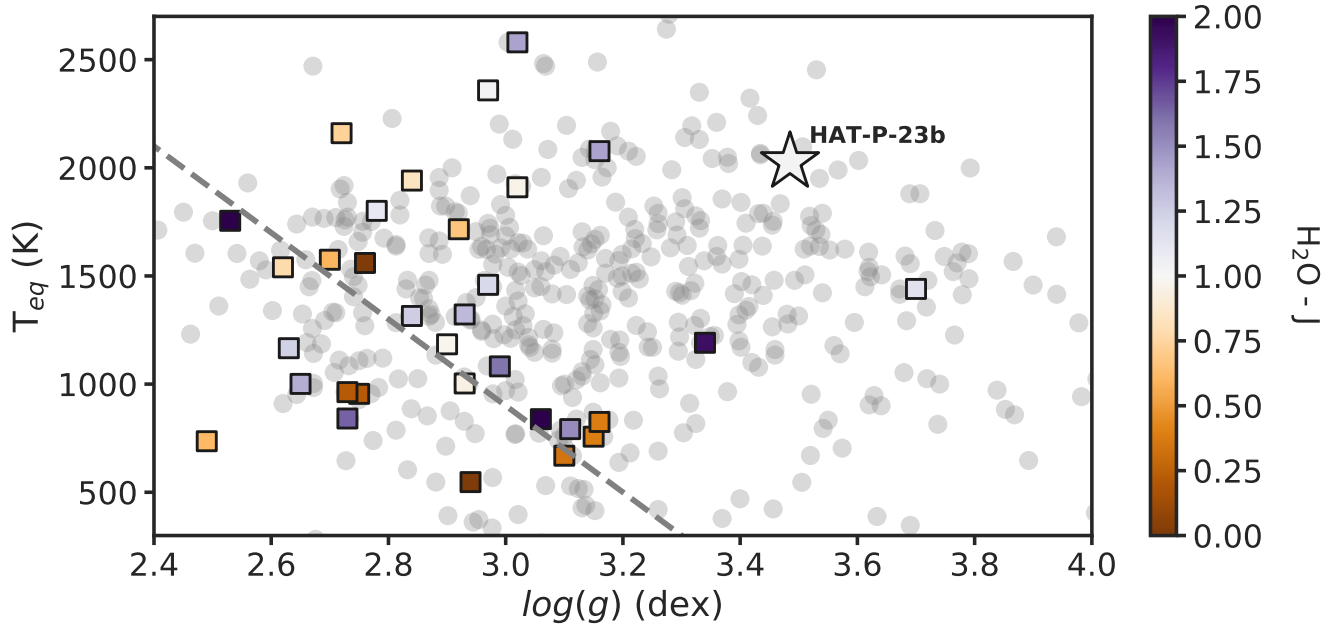


**Figure 9.** Measured surface gravity vs. equilibrium temperature of re-analyzed exoplanets (colored squares) from Figure 13 of Alam et al. (2020), color coded by water feature strength. Exoplanets with mass and radius measurements are shown for comparison in grey. We overplot HAT-P-23b for comparison to show its unique position in this parameter space and motivate future space-based missions to measure its  $1.4 \mu\text{m}$   $\text{H}_2\text{O}$  bandhead amplitude, which will provide a good test for the delineation between clear and cloudy exoplanets based on water feature strength proposed by Stevenson (2016) (gray dashed line). (</>)

transit events between 2016 and 2018, spanning a total wavelength coverage of 5,200 Å–9,269 Å. We summarize our findings from this combined transmission spectrum below:

- The average precision we achieve per wavelength bin (247 ppm) is comparable to the predicted 5-scale-height signal assuming a hydrogen-dominated atmosphere (384 ppm). We note that the actual signal could be appreciably smaller, requiring additional transits to build sufficient signal to make any strong claims about the planet’s atmosphere.
- We perform a generic forward modeling analysis with ATMO to begin this characterization. We find that the best fitting model favors a high equilibrium temperature ( $T_{\text{eq}} \approx 2,500$  K), which we note may be driven by potential TiO/VO features present in the transmission spectrum.
- We perform a comprehensive retrieval analysis exploring all combinations of atomic/molecular species and atmosphere types tested. Informed by photometric activity data, we find a consistent trend marginally favoring the presence of TiO in the atmosphere of HAT-P-23b, but note that this trend is not as strong when fitting for the mean transit depth.
- We place HAT-P-23b in the context of other exoplanets that have been analyzed in terms of their measured surface gravities and equilibrium temperatures in the search for potential predictive trends in the cloudiness vs. clarity of their atmospheres. With our current results favoring a clear atmosphere with TiO for HAT-P-23b, the planet falls in the predicted location for clear planets by [Stevenson \(2016\)](#).
- Finally, we recommend that because this suggested trend is based on measurements made in the near-

IR, this unique target (due to its large surface gravity) should be followed-up with HST to provide this necessary data and provide a good test for this potential trend.

#### ACKNOWLEDGMENTS

We thank the anonymous referee and data editor for helpful comments and feedback. This paper includes data gathered with the 6.5 meter Magellan Telescopes located at Las Campanas Observatory, Chile. We thank Jennifer Fienco, the Las Campanas Observatory staff, and the observing personnel for providing the facilities and guidance necessary for making the collection of this high-quality dataset possible. This research has made use of the VizieR catalogue access tool, CDS, Strasbourg, France ([Ochsenbein et al. 2000](#)). A.J. acknowledges support from ANID – Millennium Science Initiative – ICN12\_009. The results reported herein benefited from collaborations and/or information exchange within NASA’s Nexus for Exoplanet System Science (NExSS) research coordination network sponsored by NASA’s Science Mission Directorate, and funding through the NExSS Earths in Other Solar System (PI: Apai) and ACCESS (PI: López-Morales) teams. ICW and MLM thank the Brinson Foundation for supporting this project. B.V.R. thanks the Heising-Simons Foundation for support. This research used computing resources from the Smithsonian Institution High Performance Cluster (SI/HPC).

*Software:* Astropy ([Astropy Collaboration et al. 2013, 2018](#)), batman ([Kreidberg 2015](#)), george ([Ambikasaran et al. 2015](#)), multineest ([Feroz & Hobson 2008; Feroz et al. 2009, 2019](#)), NumPy ([Harris et al. 2020](#)), SciPy ([Virtanen et al. 2020](#)), corner ([Foreman-Mackey 2016](#)), jupyter ([Kluyver et al. 2016](#)), pandas ([Wes McKinney 2010](#)), matplotlib ([Hunter 2007](#)), seaborn ([Waskom et al. 2020](#)), Measurements.jl ([Giordano 2016](#))

#### REFERENCES

- Aigrain, S., Pont, F., & Zucker, S. 2012, [MNRAS](#), **419**, 3147
- Alam, M. K., Nikolov, N., López-Morales, M., et al. 2018, [AJ](#), **156**, 298
- Alam, M. K., López-Morales, M., Nikolov, N., et al. 2020, [AJ](#), **160**, 51
- Alam, M. K., López-Morales, M., MacDonald, R. J., et al. 2021, [ApJL](#), **906**, L10
- Ambikasaran, S., Foreman-Mackey, D., Greengard, L., Hogg, D. W., & O’Neil, M. 2015, [IEEE Transactions on Pattern Analysis and Machine Intelligence](#), **38**, 252
- Amundsen, D. S., Baraffe, I., Tremblin, P., et al. 2014, [A&A](#), **564**, A59
- Apai, D., Rackham, B. V., Giampapa, M. S., et al. 2018, ArXiv e-prints, arXiv:1803.08708
- Astropy Collaboration, Robitaille, T. P., Tollerud, E. J., et al. 2013, [A&A](#), **558**, A33
- Astropy Collaboration, Price-Whelan, A. M., SipHocz, B. M., et al. 2018, [aj](#), **156**, 123
- Bakos, G. Á., Hartman, J., Torres, G., et al. 2011, [ApJ](#), **742**, 116

- Barlow, R. 2003, arXiv e-prints, physics/0306138
- Berta, Z. K., Charbonneau, D., Bean, J., et al. 2011, *ApJ*, **736**, 12
- Bixel, A., Rackham, B. V., Apai, D., et al. 2019, *AJ*, **157**, 68
- Bonomo, A. S., Desidera, S., Benatti, S., et al. 2017, *A&A*, **602**, A107
- Buchner, J., Georgakakis, A., Nandra, K., et al. 2014, *A&A*, **564**, A125
- Carter, A. L., Nikolov, N., Sing, D. K., et al. 2020, *MNRAS*, **494**, 5449
- Charbonneau, D., Brown, T. M., Noyes, R. W., & Gilliland, R. L. 2002, *ApJ*, **568**, 377
- Ciceri, S., Mancini, L., Southworth, J., et al. 2015, *A&A*, **577**, A54
- Dressler, A., Hare, T., Bigelow, B. C., & Osip, D. J. 2006, in *Proc. SPIE, Vol. 6269, Society of Photo-Optical Instrumentation Engineers (SPIE) Conference Series*, 62690F
- Drummond, B., Tremblin, P., Baraffe, I., et al. 2016, *A&A*, **594**, A69
- Espinoza, N. 2018, *Research Notes of the American Astronomical Society*, **2**, 209
- Espinoza, N., Fortney, J. J., Miguel, Y., Thorngren, D., & Murray-Clay, R. 2017, *ApJ*, **838**, L9
- Espinoza, N., & Jordán, A. 2016, *MNRAS*, **457**, 3573
- Espinoza, N., Rackham, B. V., Jordán, A., et al. 2019, *MNRAS*, **482**, 2065
- Feroz, F., & Hobson, M. P. 2008, *MNRAS*, **384**, 449
- Feroz, F., Hobson, M. P., & Bridges, M. 2009, *MNRAS*, **398**, 1601
- Feroz, F., Hobson, M. P., Cameron, E., & Pettitt, A. N. 2019, *The Open Journal of Astrophysics*, **2**, 10
- Fischer, P. D., Knutson, H. A., Sing, D. K., et al. 2016, *ApJ*, **827**, 19
- Foreman-Mackey, D. 2016, *The Journal of Open Source Software*, **1**, 24
- Fraine, J., Deming, D., Benneke, B., et al. 2014, *Nature*, **513**, 526
- Fu, G., Deming, D., Knutson, H., et al. 2017, *ApJL*, **847**, L22
- Gaia Collaboration, Brown, A. G. A., Vallenari, A., et al. 2018, *A&A*, **616**, A1
- Gibson, N. P., Aigrain, S., Barstow, J. K., et al. 2013, *MNRAS*, **436**, 2974
- Gibson, N. P., Aigrain, S., Roberts, S., et al. 2012, *MNRAS*, **419**, 2683
- Giordano, M. 2016, ArXiv e-prints, [arXiv:1610.08716](https://arxiv.org/abs/1610.08716) [[physics.data-an](https://arxiv.org/abs/1610.08716)]
- Goyal, J. M., Wakeford, H. R., Mayne, N. J., et al. 2019, *MNRAS*, **482**, 4503
- Goyal, J. M., Mayne, N., Sing, D. K., et al. 2018, *MNRAS*, **474**, 5158
- Harris, C. R., Millman, K. J., van der Walt, S. J., et al. 2020, *Nature*, **585**, 357–362
- Helling, C., Lee, G., Dobbs-Dixon, I., et al. 2016, *MNRAS*, **460**, 855
- Heng, K. 2016, *ApJL*, **826**, L16
- Hunter, J. D. 2007, *Computing In Science & Engineering*, **9**, 90
- Jordán, A., Espinoza, N., Rabus, M., et al. 2013, *ApJ*, **778**, 184
- Kipping, D. M. 2013, *MNRAS*, **435**, 2152
- Kirk, J., López-Morales, M., Wheatley, P. J., et al. 2019, *AJ*, **158**, 144
- Kirk, J., Wheatley, P. J., Louden, T., et al. 2018, *MNRAS*, **474**, 876
- Kluyver, T., Ragan-Kelley, B., Pérez, F., et al. 2016, in *Positioning and Power in Academic Publishing: Players, Agents and Agendas*, ed. F. Loizides & B. Schmidt (Netherlands: IOS Press), 87
- Kochanek, C. S., Shappee, B. J., Stanek, K. Z., et al. 2017, *Publications of the Astronomical Society of the Pacific*, **129**, 104502
- Kreidberg, L. 2015, *PASP*, **127**, 1161
- Kreidberg, L., Bean, J. L., Désert, J.-M., et al. 2014, *ApJL*, **793**, L27
- MacDonald, R. J., Goyal, J. M., & Lewis, N. K. 2020, *ApJL*, **893**, L43
- Marley, M. S., Ackerman, A. S., Cuzzi, J. N., & Kitzmann, D. 2013, *Clouds and hazes in exoplanet atmospheres*, Space Science Series (Phoenix: University of Arizona Press), 367
- McCullough, P. R., Crouzet, N., Deming, D., & Madhusudhan, N. 2014, *The Astrophysical Journal*, **791**, 55
- McGruder, C. D., López-Morales, M., Espinoza, N., et al. 2020, *AJ*, **160**, 230
- Miller-Ricci, E., Seager, S., & Sasselov, D. 2009, *ApJ*, **690**, 1056
- Mordasini, C., van Boekel, R., Mollière, P., Henning, T., & Benneke, B. 2016, *ApJ*, **832**, 41
- Moses, J. I., Line, M. R., Visscher, C., et al. 2013, *ApJ*, **777**, 34
- Nielsen, E. L., De Rosa, R. J., Macintosh, B., et al. 2019, arXiv e-prints, [arXiv:1904.05358](https://arxiv.org/abs/1904.05358)
- Nikolov, N., Sing, D. K., Gibson, N. P., et al. 2016, *ApJ*, **832**, 191
- Nikolov, N., Sing, D. K., Fortney, J. J., et al. 2018, *Nature*, **557**, 526
- Öberg, K. I., Boamah, M. D., Fayolle, E. C., et al. 2013, *ApJ*, **771**, 95

- Ochsenbein, F., Bauer, P., & Marcout, J. 2000, [A&AS](#), **143**, 23
- O'Rourke, J. G., Knutson, H. A., Zhao, M., et al. 2014, [ApJ](#), **781**, 109
- Oshagh, M., Santos, N. C., Ehrenreich, D., et al. 2014, [A&A](#), **568**, A99
- Pinhas, A., Madhusudhan, N., Gandhi, S., & MacDonald, R. 2019, [MNRAS](#), **482**, 1485
- Pluriel, W., Zingales, T., Leconte, J., & Parmentier, V. 2020, [A&A](#), **636**, A66
- Pont, F., Knutson, H., Gilliland, R. L., Moutou, C., & Charbonneau, D. 2008, [MNRAS](#), **385**, 109
- Pont, F., Sing, D. K., Gibson, N. P., et al. 2013, [MNRAS](#), **432**, 2917
- Rackham, B., Espinoza, N., Apai, D., et al. 2017, [ApJ](#), **834**, 151
- Rackham, B. V., Apai, D., & Giampapa, M. S. 2018, [ApJ](#), **853**, 122
- . 2019, [AJ](#), **157**, 96
- Rasmussen, C. E., & Williams, C. K. I. 2005, *Gaussian Processes for Machine Learning (Adaptive Computation and Machine Learning)* (The MIT Press)
- Sada, P. V., & Ramón-Fox, F. G. 2016, [PASP](#), **128**, 024402
- Schrijver, C. J. 2020, [ApJ](#), **890**, 121
- Shapsee, B. J., Prieto, J. L., Grupe, D., et al. 2014, [The Astrophysical Journal](#), **788**, 48
- Showman, A., Cho, J., & Menou, K. 2009, arXiv: Earth and Planetary Astrophysics
- Sing, D. K. 2018, arXiv e-prints, arXiv:1804.07357
- Sing, D. K., Désert, J.-M., Lecavelier Des Etangs, A., et al. 2009, [A&A](#), **505**, 891
- Sing, D. K., Pont, F., Aigrain, S., et al. 2011, [MNRAS](#), **416**, 1443
- Sing, D. K., Lecavelier des Etangs, A., Fortney, J. J., et al. 2013, [MNRAS](#), **436**, 2956
- Sing, D. K., Fortney, J. J., Nikolov, N., et al. 2016, [Nature](#), **529**, 59
- Stassun, K. G., Oelkers, R. J., Paegert, M., et al. 2019, [AJ](#), **158**, 138
- Stevenson, K. B. 2016, [ApJL](#), **817**, L16
- Tremblin, P., Amundsen, D. S., Mourier, P., et al. 2015, [ApJL](#), **804**, L17
- Virtanen, P., Gommers, R., Oliphant, T. E., et al. 2020, [Nature Methods](#), **17**, 261
- Wakeford, H. R., & Sing, D. K. 2015, [A&A](#), **573**, A122
- Wakeford, H. R., Wilson, T. J., Stevenson, K. B., & Lewis, N. K. 2019, [Research Notes of the American Astronomical Society](#), **3**, 7
- Wakeford, H. R., Stevenson, K. B., Lewis, N. K., et al. 2017, [ApJ](#), **835**, L12
- Wakeford, H. R., Sing, D. K., Deming, D., et al. 2018, [AJ](#), **155**, 29
- Wakeford, H. R., Sing, D. K., Stevenson, K. B., et al. 2020, [AJ](#), **159**, 204
- Waskom, M., Botvinnik, O., Gelbart, M., et al. 2020, *seaborn: Statistical data visualization*
- Weaver, I. C., López-Morales, M., Espinoza, N., et al. 2020, [AJ](#), **159**, 13
- Wes McKinney. 2010, in *Proceedings of the 9th Python in Science Conference*, ed. Stéfan van der Walt & Jarrod Millman, 56
- Zhang, Z., Zhou, Y., Rackham, B. V., & Apai, D. 2018, [AJ](#), **156**, 178

## APPENDIX

Here we provide additional figures and tables referenced in the main text.

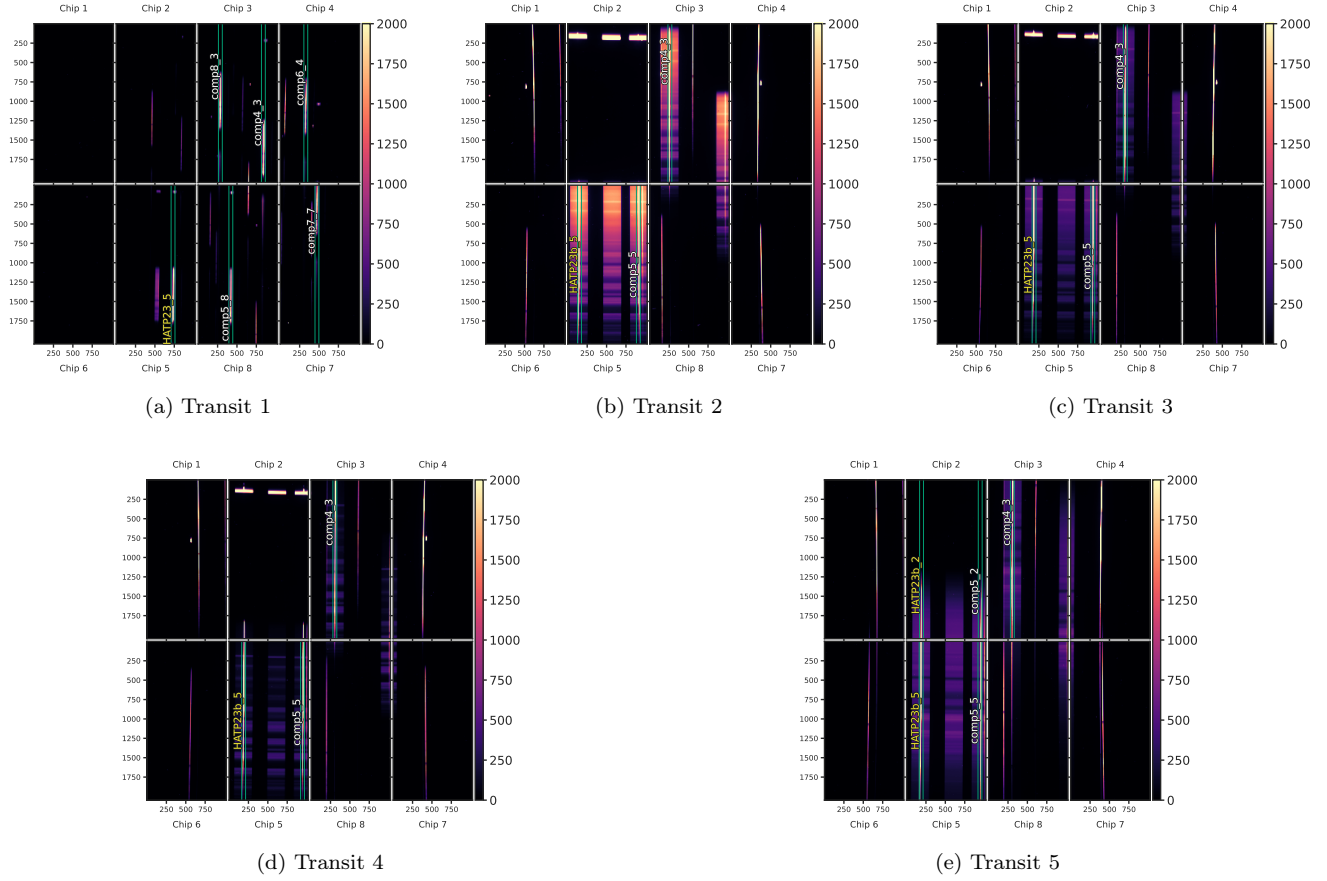


**Figure 10.** Sample science frames of 2D spectra collected from all nights on *Magellan/IMACS* used in our final analysis, colored by counts. The presence of a contaminating source in the slit for comp5 set the maximum aperture size for all nights (show in green). (</>)



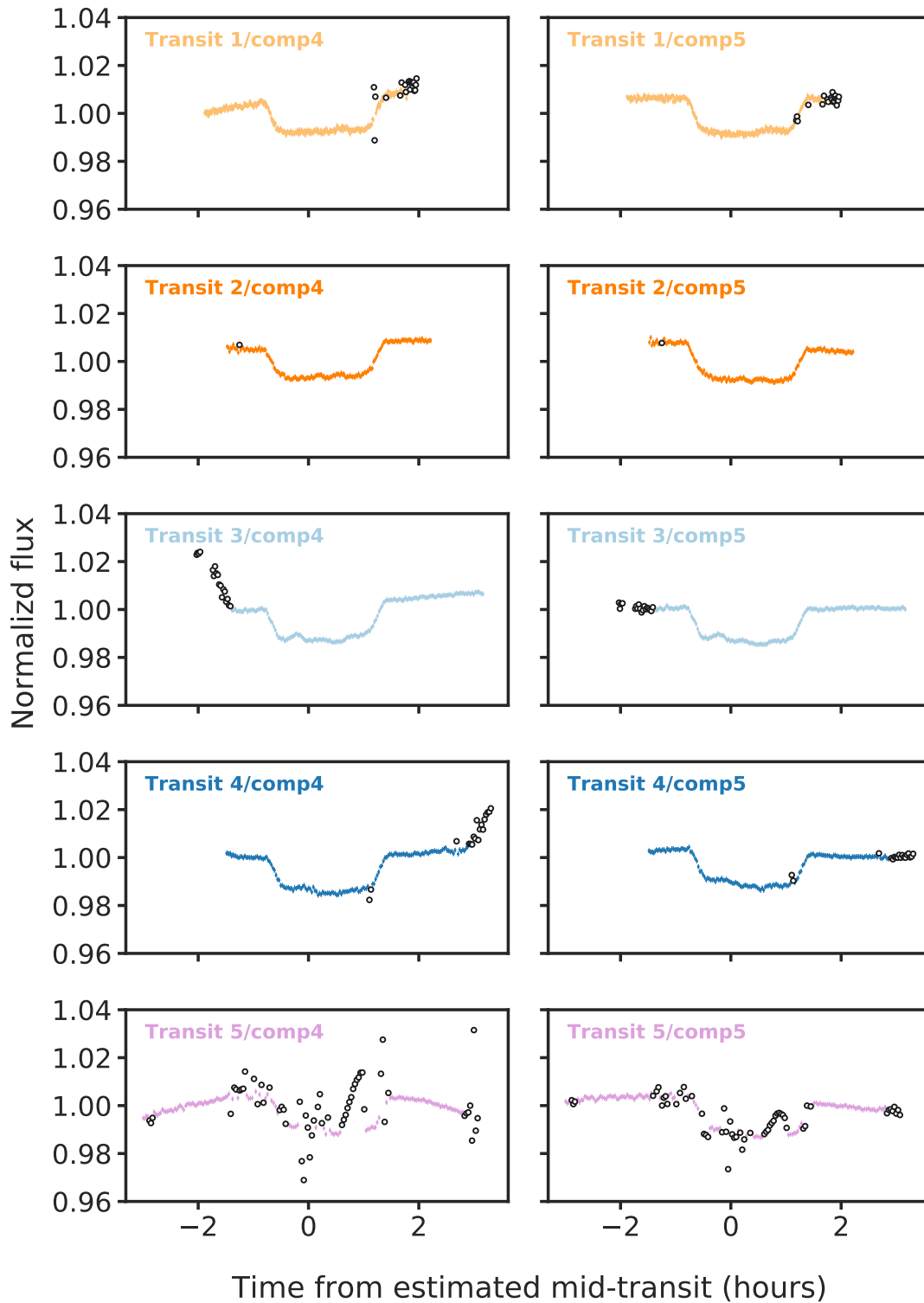


**Figure 11.** Divided white-light curves for each night used in our final analysis. The raw WLC for HAT-P-23 divided by the raw WLC for comp4 and comp5 is shown in the first and second column, respectively. The union of identified outliers for each night is highlighted in white circles. (</>)

**Table 5.** Wavelength bins (in Å) used in main analysis.

Wav start	Wav end	Wav diff	Wav cen
5200.0	5400.0	200.0	5300.0
5400.0	5600.0	200.0	5500.0
5600.0	5800.0	200.0	5700.0
5800.0	5985.8	185.8	5892.9
5985.8	6185.8	200.0	6085.8
6655.0	6855.0	200.0	6755.0
6855.0	7055.0	200.0	6955.0
7055.0	7255.0	200.0	7155.0
7255.0	7455.0	200.0	7355.0
7455.0	7655.0	200.0	7555.0
7655.0	7709.0	54.0	7682.0
7709.0	7909.0	200.0	7809.0
7909.0	8109.0	200.0	8009.0
8109.0	8269.0	160.0	8189.0
8269.0	8469.0	200.0	8369.0
8469.0	8669.0	200.0	8569.0
8669.0	8869.0	200.0	8769.0
8869.0	9069.0	200.0	8969.0
9069.0	9269.0	200.0	9169.0

**Table 6.** Wavelength bins (in Å) used in Figure 5.

Wav start	Wav end	Wav diff	Wav cen
5780.4	5825.4	45.0	5802.9
5825.4	5870.4	45.0	5847.9
5870.4	5915.4	45.0	5892.9
5915.4	5960.4	45.0	5937.9
5960.4	6005.4	45.0	5982.9
7657.0	7667.0	10.0	7662.0
7667.0	7677.0	10.0	7672.0
7677.0	7687.0	10.0	7682.0
7687.0	7697.0	10.0	7692.0
7697.0	7707.0	10.0	7702.0
8089.0	8129.0	40.0	8109.0
8129.0	8169.0	40.0	8149.0
8169.0	8209.0	40.0	8189.0
8209.0	8249.0	40.0	8229.0
8249.0	8289.0	40.0	8269.0

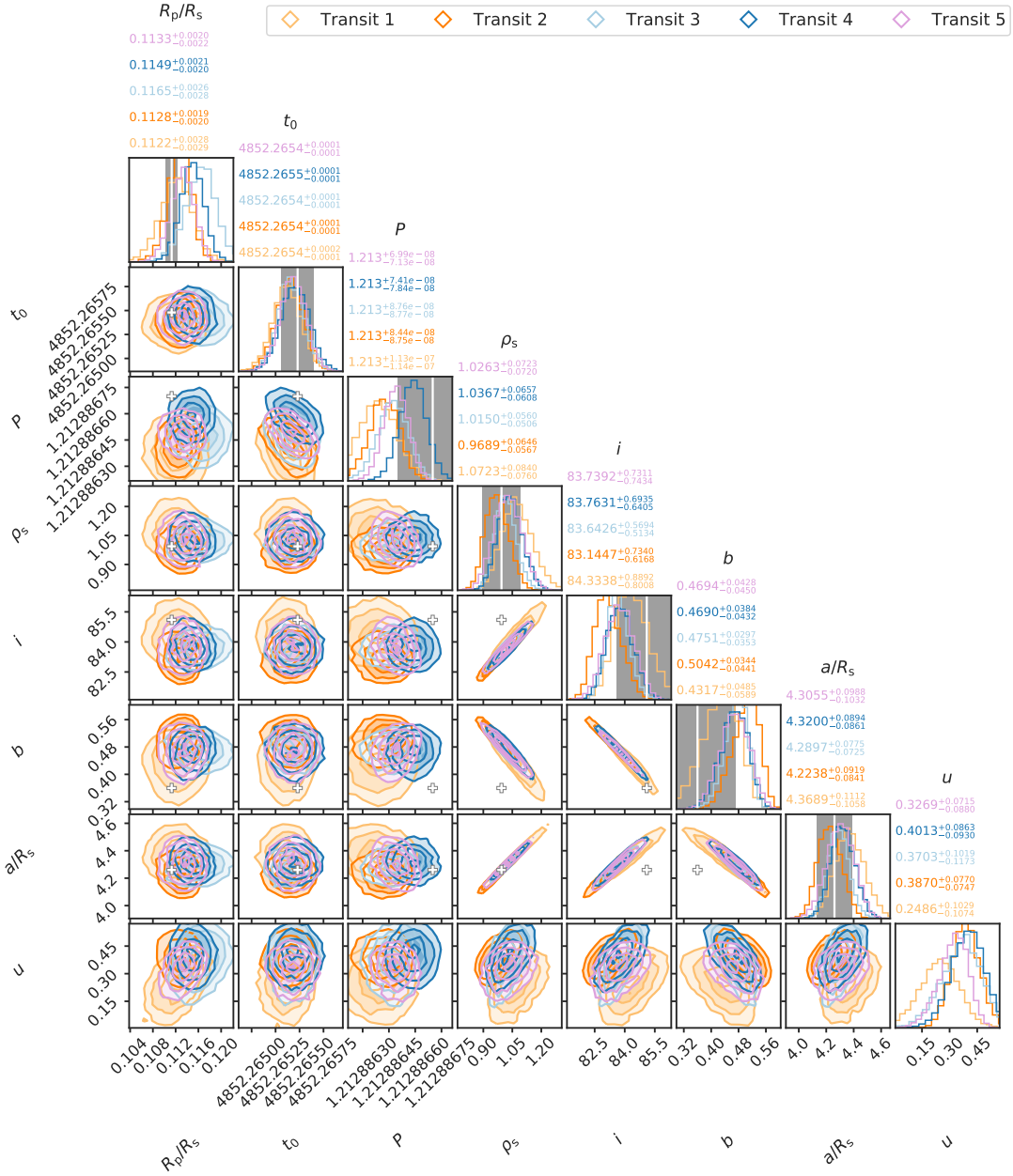


**Figure 12.** Detrended white-light curve corner plots for all nights used in our final analysis, color-coded by transit. The reported values (highlighted, white crosses) are from a self-consistent analysis (described in Section 1) of the most recent transit and RV data available. The associated WLCs are presented in Figure 2 and tabulated values of our best-fit parameters are shared in Table 3. (</>)

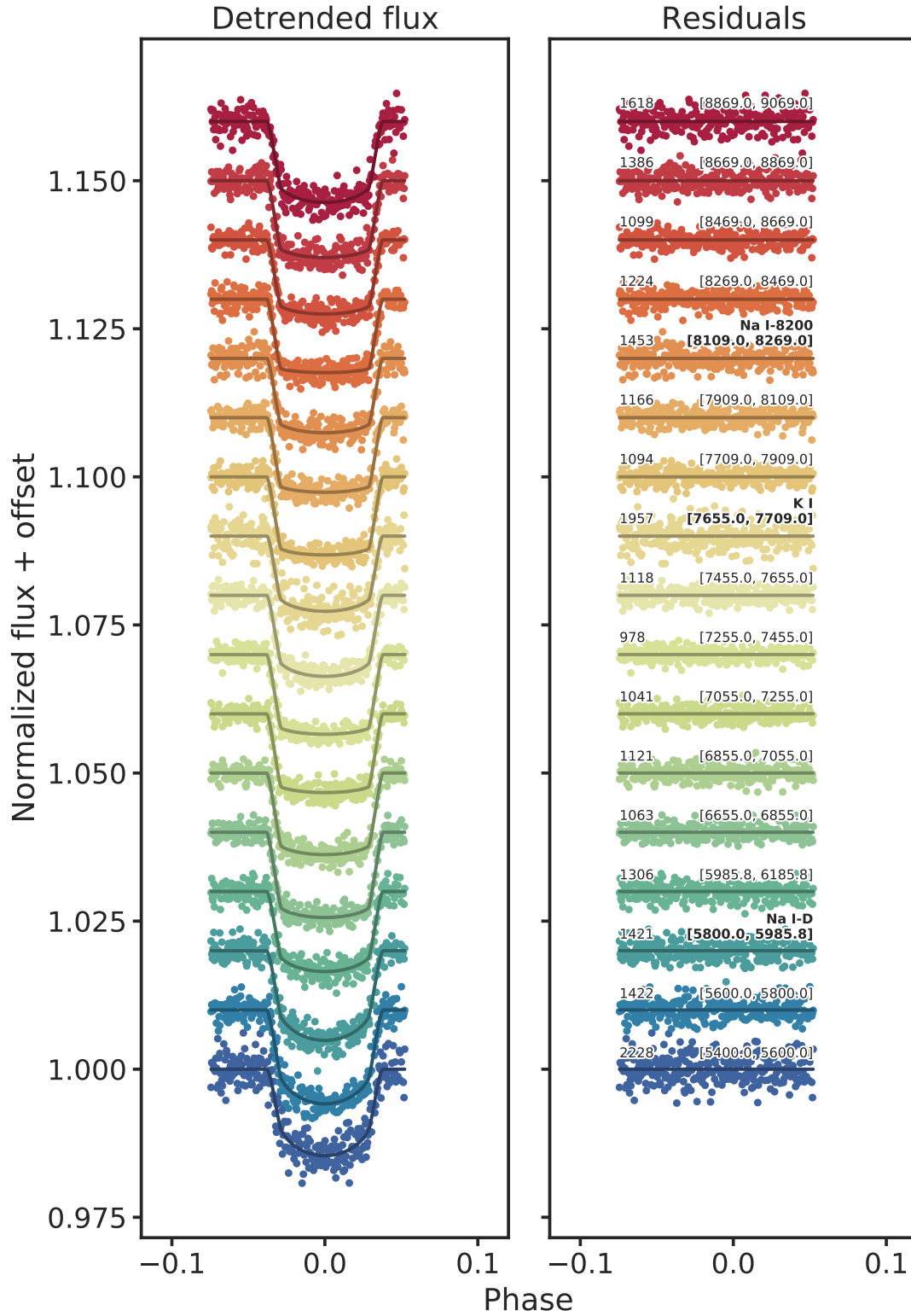


**Figure 13.** Detrended binned light curves for Transit 1 used to build the final transmission spectrum in Figure 4. The standard deviation in the residuals and corresponding wavelength bin are annotated on the left and right side of the right-hand panel, respectively. The tabulated data for these binned light curves are available in Table 7. (</>)

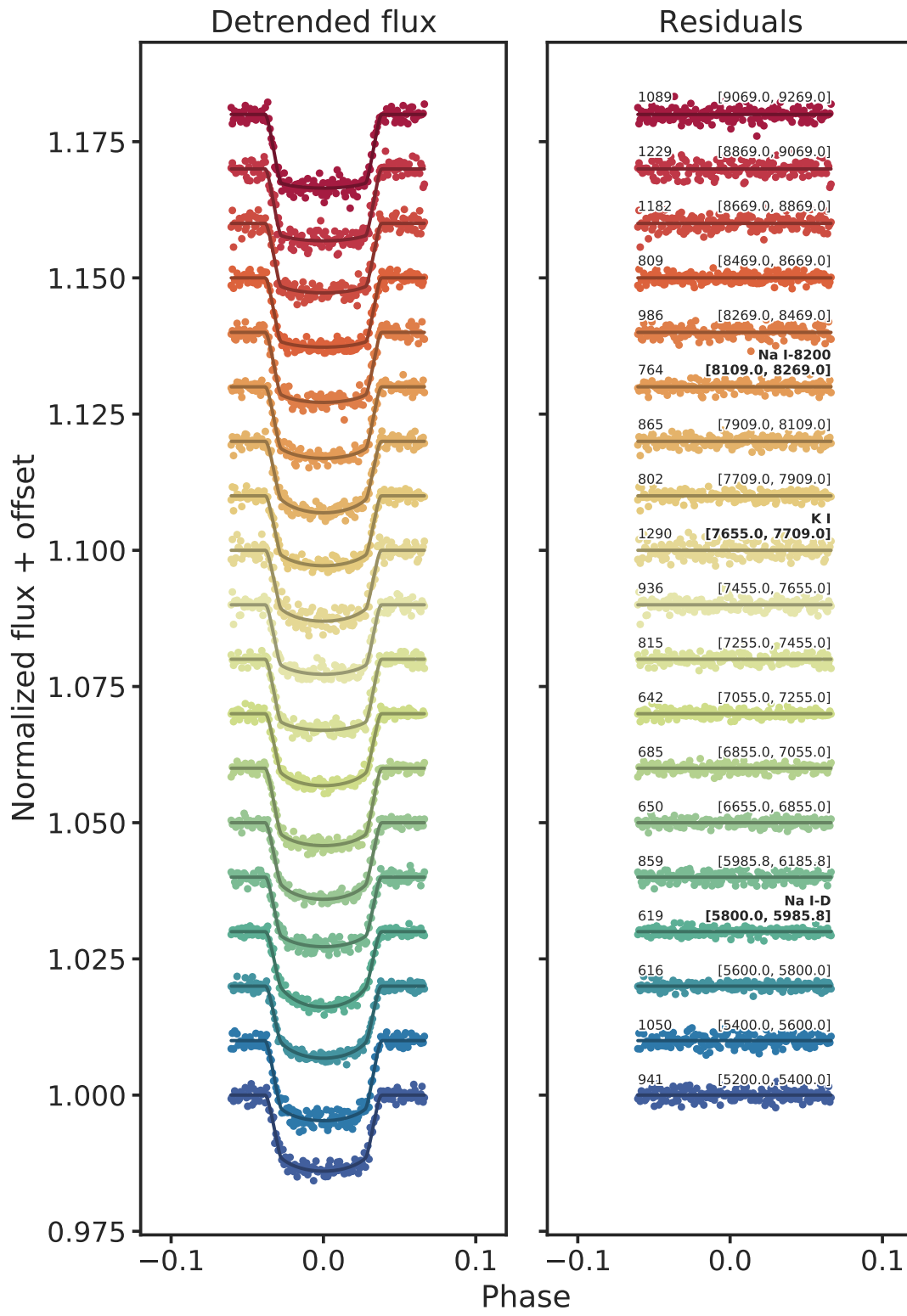


Figure 14. Same as Figure 13, but for Transit 2. (</>)



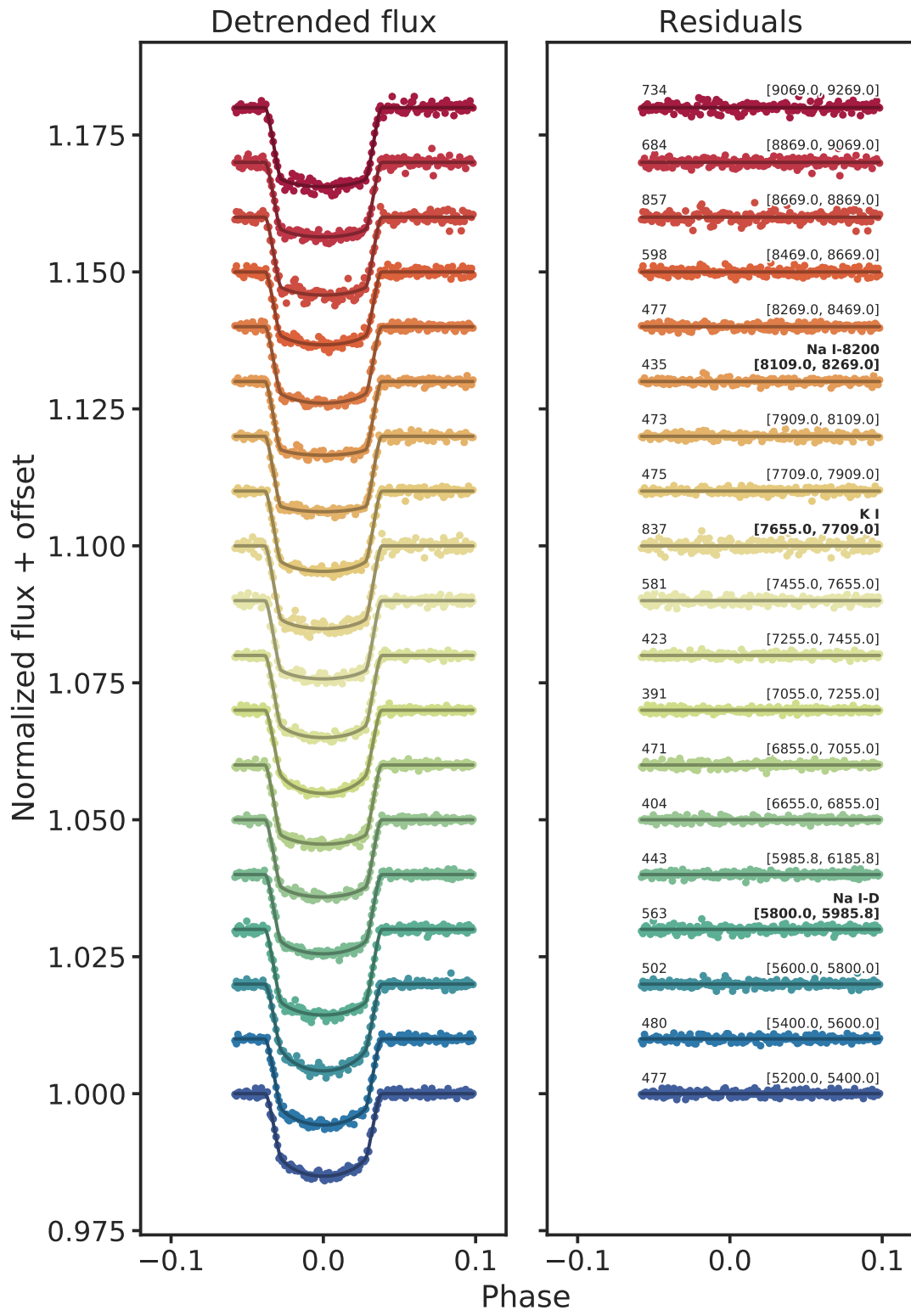


Figure 15. Same as Figure 13, but for Transit 3. (</>)

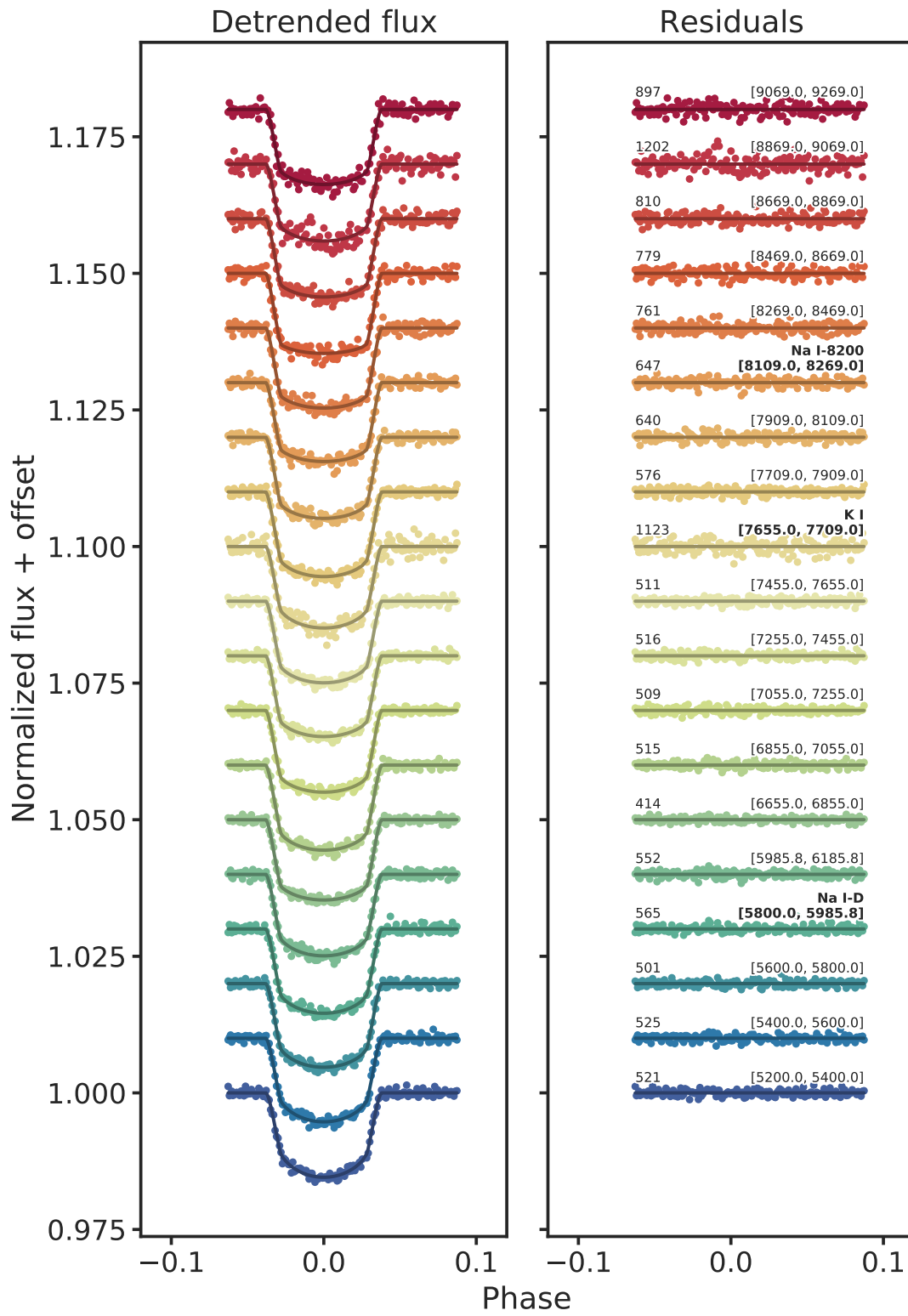


Figure 16. Same as Figure 13, but for Transit 4. (</>)

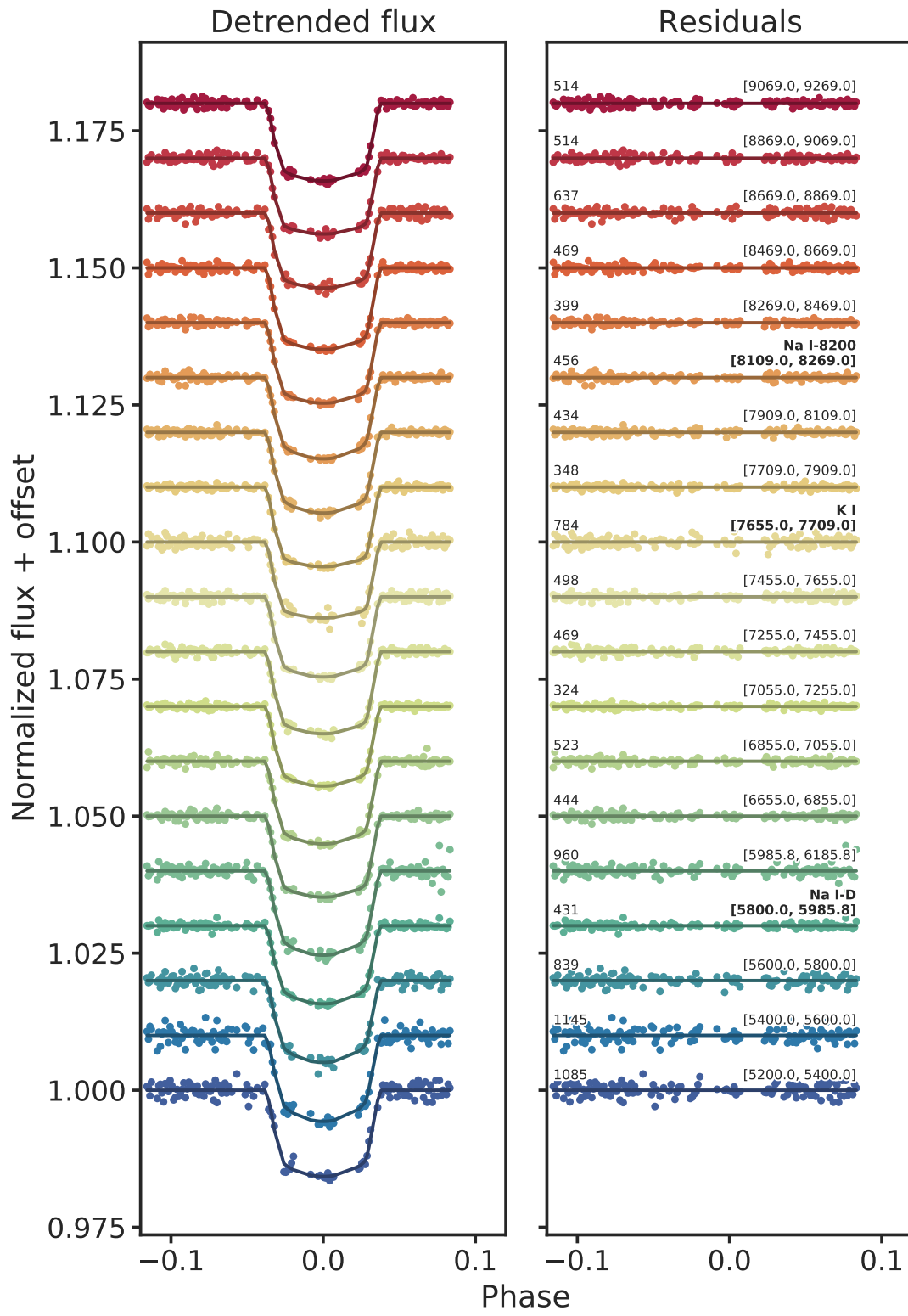


Figure 17. Same as Figure 13, but for Transit 5. (</>)

**Table 7.** Final offset, tabulated transit depths (in ppm) from Figure 4, corresponding to binned light curves in Figures 13 – 17. For reference, the weighted mean white-light curve transit depth is  $12,966 \text{ ppm} \pm 228 \text{ ppm}$ .

Wavelength (Å)	Transit 1	Transit 2	Transit 3	Transit 4	Transit 5	Combined
5400.0 – 5600.0	$13100^{+1300}_{-1400}$	$13900^{+300}_{-300}$	$13600^{+600}_{-600}$	$13300^{+600}_{-600}$	$14000^{+600}_{-600}$	$13800 \pm 200$
5600.0 – 5800.0	$14200^{+1400}_{-1400}$	$12000^{+1200}_{-1100}$	$13300^{+700}_{-700}$	$13300^{+600}_{-600}$	$13400^{+500}_{-500}$	$13300 \pm 300$
5800.0 – 5985.8	$13600^{+1100}_{-1200}$	$11900^{+1100}_{-1000}$	$14000^{+700}_{-800}$	$13700^{+400}_{-400}$	$13000^{+800}_{-700}$	$13500 \pm 300$
5985.8 – 6185.8	$12800^{+1000}_{-1000}$	$12300^{+1000}_{-500}$	$12800^{+1200}_{-1300}$	$13200^{+500}_{-500}$	$14000^{+700}_{-700}$	$13200 \pm 300$
6655.0 – 6855.0	$14000^{+900}_{-800}$	$13000^{+600}_{-700}$	$12600^{+500}_{-600}$	$13200^{+600}_{-600}$	$13800^{+400}_{-400}$	$13300 \pm 200$
6855.0 – 7055.0	$13100^{+900}_{-900}$	$13400^{+400}_{-500}$	$13000^{+600}_{-600}$	$14000^{+600}_{-600}$	$14100^{+400}_{-400}$	$13700 \pm 200$
7055.0 – 7255.0	$13000^{+700}_{-700}$	$12600^{+900}_{-900}$	$12900^{+700}_{-700}$	$13800^{+600}_{-600}$	$13800^{+300}_{-300}$	$13600 \pm 200$
7255.0 – 7455.0	$13400^{+800}_{-700}$	$12500^{+600}_{-600}$	$13500^{+600}_{-600}$	$13300^{+500}_{-400}$	$14300^{+200}_{-300}$	$13800 \pm 200$
7455.0 – 7655.0	$12900^{+1000}_{-1000}$	$12200^{+600}_{-600}$	$12800^{+600}_{-600}$	$13400^{+400}_{-400}$	$14000^{+500}_{-500}$	$13200 \pm 200$
7655.0 – 7709.0	$12200^{+900}_{-800}$	$12300^{+700}_{-700}$	$13800^{+1000}_{-1000}$	$13500^{+700}_{-700}$	$13200^{+500}_{-500}$	$13000 \pm 300$
7709.0 – 7909.0	$13100^{+800}_{-800}$	$12200^{+600}_{-600}$	$13000^{+500}_{-400}$	$14000^{+700}_{-700}$	$14100^{+400}_{-400}$	$13400 \pm 200$
7909.0 – 8109.0	$12400^{+600}_{-600}$	$12200^{+700}_{-700}$	$12600^{+500}_{-500}$	$13600^{+500}_{-600}$	$13600^{+400}_{-400}$	$13000 \pm 200$
8109.0 – 8269.0	$12500^{+400}_{-300}$	$12600^{+700}_{-800}$	$12300^{+500}_{-500}$	$13200^{+500}_{-500}$	$13700^{+500}_{-500}$	$12900 \pm 200$
8269.0 – 8469.0	$12600^{+400}_{-400}$	$12600^{+800}_{-900}$	$12400^{+400}_{-400}$	$13400^{+500}_{-500}$	$13800^{+400}_{-400}$	$13100 \pm 200$
8469.0 – 8669.0	$12300^{+600}_{-600}$	$12400^{+600}_{-500}$	$11800^{+500}_{-500}$	$13600^{+500}_{-500}$	$13400^{+400}_{-400}$	$12700 \pm 200$
8669.0 – 8869.0	$12600^{+700}_{-600}$	$12300^{+400}_{-500}$	$12800^{+400}_{-400}$	$12900^{+400}_{-400}$	$12800^{+700}_{-700}$	$12700 \pm 200$
8869.0 – 9069.0	$13100^{+800}_{-900}$	$12800^{+400}_{-500}$	$12300^{+600}_{-500}$	$12700^{+400}_{-300}$	$13000^{+600}_{-600}$	$12700 \pm 200$

**Table 8.** Same as Table 7, but for the wavelength bin scheme centered around each species investigated for Figure 5. The resulting weighted mean white-light curve depth is  $12,948 \text{ ppm} \pm 241 \text{ ppm}$ .

Wavelength (Å)	Transit 1	Transit 2	Transit 3	Transit 4	Transit 5	Combined
5780.4 – 5825.4	$13800^{+1600}_{-1600}$	$11800^{+1300}_{-1300}$	$12700^{+700}_{-700}$	$14000^{+400}_{-400}$	$13800^{+800}_{-800}$	$13600 \pm 300$
5825.4 – 5870.4	$14100^{+1500}_{-1600}$	$12500^{+700}_{-1000}$	$13000^{+700}_{-700}$	$13600^{+400}_{-400}$	$14300^{+900}_{-1000}$	$13500 \pm 300$
5870.4 – 5915.4	$12400^{+1400}_{-1400}$	$12200^{+1400}_{-1400}$	$13000^{+1000}_{-1200}$	$13300^{+500}_{-600}$	$13800^{+800}_{-800}$	$13300 \pm 400$
5915.4 – 5960.4	$13100^{+1400}_{-1400}$	$12900^{+1300}_{-1300}$	$13500^{+1100}_{-1100}$	$14000^{+400}_{-500}$	$13900^{+600}_{-600}$	$13800 \pm 300$
5960.4 – 6005.4	$13300^{+1700}_{-1700}$	$12000^{+700}_{-700}$	$12300^{+800}_{-900}$	$13900^{+300}_{-300}$	$13800^{+700}_{-900}$	$13500 \pm 300$
7657.0 – 7667.0	$12500^{+1500}_{-1400}$	$12100^{+1700}_{-1600}$	$12600^{+1800}_{-1800}$	$12800^{+900}_{-800}$	$12800^{+1100}_{-1000}$	$12600 \pm 500$
7667.0 – 7677.0	$12500^{+1500}_{-1400}$	$11200^{+1100}_{-1100}$	$13700^{+1400}_{-1500}$	$12500^{+600}_{-700}$	$13000^{+800}_{-800}$	$12500 \pm 400$
7677.0 – 7687.0	$12700^{+1400}_{-1300}$	$11700^{+1200}_{-1200}$	$12300^{+1100}_{-1100}$	$13100^{+700}_{-800}$	$13700^{+800}_{-800}$	$12900 \pm 400$
7687.0 – 7697.0	$11500^{+1000}_{-1100}$	$12000^{+1400}_{-1300}$	$10500^{+900}_{-900}$	$13800^{+700}_{-700}$	$12900^{+700}_{-700}$	$12400 \pm 400$
7697.0 – 7707.0	$12100^{+1400}_{-1400}$	$11200^{+900}_{-900}$	$12800^{+1100}_{-1100}$	$14200^{+600}_{-700}$	$14500^{+700}_{-700}$	$13500 \pm 400$
8089.0 – 8129.0	$12700^{+800}_{-800}$	$12100^{+900}_{-900}$	$11600^{+500}_{-500}$	$13800^{+700}_{-700}$	$14200^{+500}_{-600}$	$12900 \pm 300$
8129.0 – 8169.0	$12500^{+600}_{-700}$	$12200^{+1300}_{-1200}$	$11500^{+500}_{-600}$	$14000^{+600}_{-600}$	$14600^{+500}_{-500}$	$13200 \pm 300$
8169.0 – 8209.0	$12700^{+1000}_{-900}$	$11800^{+1300}_{-1200}$	$11800^{+700}_{-600}$	$13000^{+600}_{-600}$	$14300^{+600}_{-600}$	$12900 \pm 300$
8209.0 – 8249.0	$14100^{+1100}_{-1100}$	$12600^{+1400}_{-1400}$	$11700^{+600}_{-600}$	$13200^{+600}_{-700}$	$14200^{+600}_{-700}$	$13100 \pm 300$
8249.0 – 8289.0	$13200^{+900}_{-900}$	$11200^{+800}_{-900}$	$10800^{+500}_{-500}$	$13000^{+600}_{-600}$	$14300^{+600}_{-700}$	$12300 \pm 300$
8669.0 – 8869.0	$12600^{+700}_{-600}$	$12300^{+400}_{-500}$	$12800^{+400}_{-400}$	$12900^{+400}_{-400}$	$12800^{+700}_{-700}$	$12700 \pm 200$
8869.0 – 9069.0	$13100^{+800}_{-900}$	$12800^{+400}_{-500}$	$12300^{+600}_{-500}$	$12700^{+400}_{-300}$	$13000^{+600}_{-600}$	$12700 \pm 200$

**Table 9.** Median and  $1\sigma$  confidence levels of the retrieved parameters for the corresponding retrieved transmission spectra in Figure 8.

Parameter	TiO (clear)	K (clear)	Na+K (clear)	Na+K (clear+cloud)	Na+K (clear+haze)	Na+K (clear+spot)
$\log P_0$	$0.5^{+4}_{-4}$	$3.4^{+2}_{-3}$	$1.4^{+3}_{-3}$	$0.8^{+3}_{-3}$	$0.5^{+3}_{-3}$	$-1.3^{+4}_{-3}$
$T$	$1751.1^{+783}_{-804}$	$620.1^{+328}_{-209}$	$1938.0^{+652}_{-779}$	$1827.7^{+714}_{-950}$	$1878.4^{+709}_{-973}$	$1393.6^{+1043}_{-886}$
$\log \text{TiO}$	$-7.1^{+4}_{-4}$	---	---	---	---	---
$\log \text{K}$	---	$-2.6^{+2}_{-3}$	$-19.4^{+8}_{-7}$	$-18.7^{+8}_{-8}$	$-18.8^{+9}_{-7}$	$-19.0^{+8}_{-7}$
$\log \text{Na}$	---	---	$-4.0^{+3}_{-3}$	$-3.9^{+3}_{-4}$	$-4.8^{+3}_{-10}$	$-15.5^{+9}_{-10}$
$\log \sigma_{\text{cloud}}$	---	---	---	$-37.7^{+10}_{-8}$	---	---
$\log a$	---	---	---	---	$-11.0^{+14}_{-13}$	---
$\gamma$	---	---	---	---	$-2.3^{+2}_{-1}$	---
$T_{\text{star}}$	---	---	---	---	---	$5906.8^{+349}_{-327}$
$T_{\text{spot}}$	---	---	---	---	---	$2200.0^{+0}_{-0}$
$f_{\text{spot}}$	---	---	---	---	---	$0.0^{+0}_{-0}$

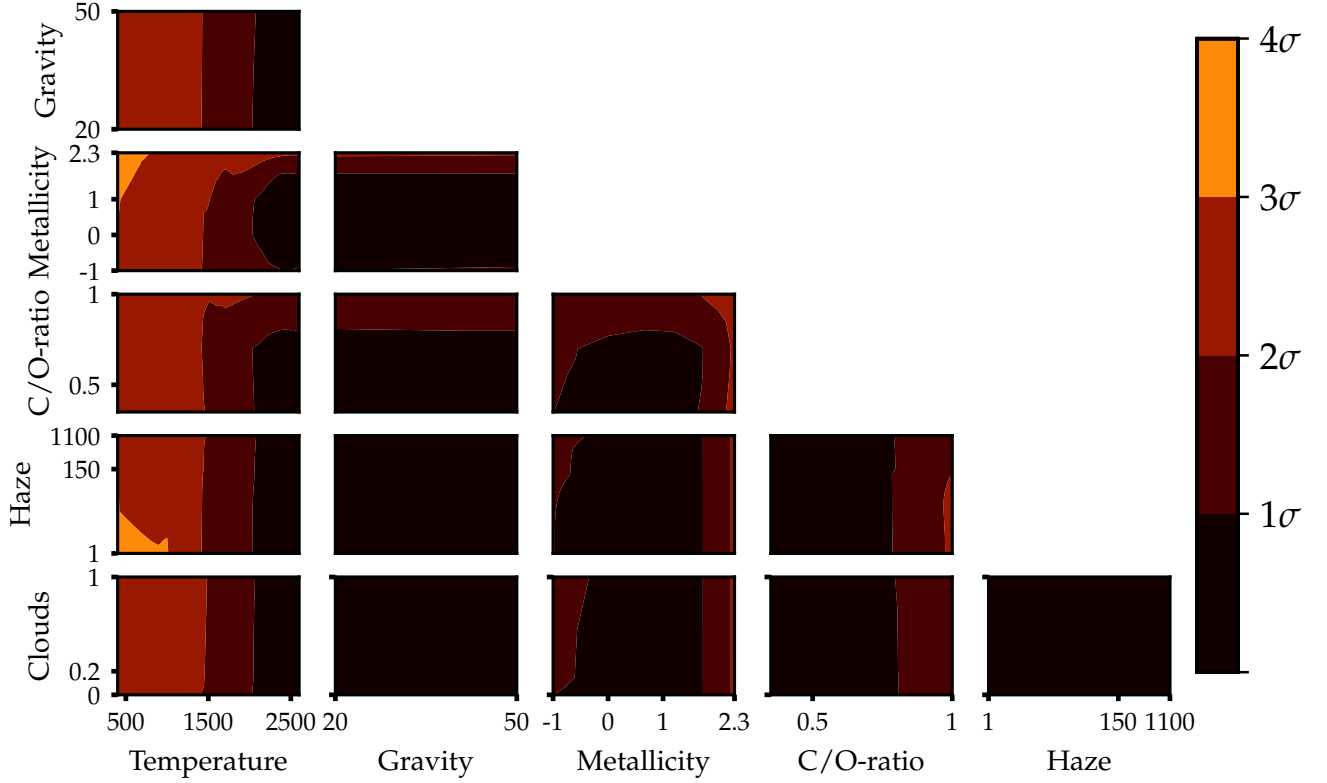


**Figure 18.**  $\chi^2$  map associated with Figure 6, showing all combinations of the above grid parameters explored in the local condensation ATMO generic grid. The colorbar on the right indicates the confidence interval of each contour. (</>)